POLITECNICO DI TORINO

Master's Degree in Materials Engineering

Master's Degree Thesis

PVDF-HFP IN ELECTROLYTES FOR SUPERCAPACITORS

Supervisors

Prof. Mara SERRAPEDE

Prof. Andrea LAMBERTI

Candidate

Vitandrea LOPEZ

MARCH 2025

Abstract

Designing flexible electrochemical double-layer capacitors (EDLCs) that can operate efficiently at high and low temperatures remains a challenge specifically related to packaging and electrolyte. The electrochemical performance of EDLCs is highly temperature dependent, and improved performance at high and low temperatures can be achieved if all components are designed for this purpose. Therefore, all solid-state symmetric EDLCs fabricated with solid-like electrolytes operating at high and low temperatures. A ionogel of poly(vinylidene fluoride-co-hexafluoropropylene) (P(VDF-HFP)) and N-butyl-N-methyl pyrrolidinium bis(trifluoromethanesulfonyl)imide (Pyr14TFSI) ionic liquid was used as the solid electrolyte and simultaneously the separator in these all-solid EDLCs. The synthesized solid ionogel with the highest ion mobility was made with a polymer to IL ratio of 1:4 in weight, which exhibits high ionic conductivity over a wide temperature range, from 0,229 mS/cm at 5°C up to 0,435 mS/cm at 70°C. Inorganic additives were used in the ionogel formulation to increase the conductivity at low temperatures or to increase the IL concentration while maintaining the robustness. Silica nanoparticles of 20-50 nm in diameter and GO flakes of 300-800 nm in length were employed as such additives, demonstrating that the polymer to IL ratio could be increased to 1:5 in weight without compromising the conductivity. These membranes were observed by FESEM to appreciate the homogeneity and the ionic conductivity was measured between 5°C and 70°C, demonstrating that the GO ionogel performed better at high temperatures while the SiO2 one was better at low temperatures. All solid-state EDLCs were then prepared with both modified ionogels and tested to withstand operating temperatures from 5°C to 70°C, under a cell voltage of 2 V with long-term galvanostatic charge-discharge cycling over 10,000 cycles. This approach paves the way for flexible leakage-less devices.

Acknowledgements

Ringrazio la mia relatrice per avermi permesso di lavorare a questa tesi. Ringrazio Francesco, per essere sempre stato disponibile ad aiutarmi durante tutto il lavoro, Pietro, per aver salvato le ultime settimane di analisi, e tutti gli altri ragazzi in ufficio per essere stati sempre molto accoglienti e d'aiuto.

Ringrazio inoltre chi c'è, chi c'è stato e chi non c'è più per avermi supportato in tutti questi anni di università.

Vi voglio un sacco di bene, anche se ogni tanto non lo vado a dimostrare.

Table of Contents

List of Tables

List of Figures

Acronyms

APIL
: Aprotic Ionic Liquid

C
: Capacitance

CCCD
: Constant Current Charge and Discharge

CNT
: Carbon Nanotubes

CV
: cyclic voltametry

DTGA
: Derivative of the TGA curve

DSC
: Differential Scanning Calorimetry

EAP
: Electroactive Polymer

EDL
: Electrical Double Layer

EDLC
: Electrical Double Layer Supercapacitor

EIS

Electrochemical Impedance Spectroscopy

ESPW

Electrochemical Stability Potential Window

FESEM

Field Emission Scanning Electron Microscope

FT-IR

Fourier Transform Infrared

G

Series of Coin Cell made using IG5 as electrolyte

GC

Gas Chromatograph

GO

Graphene Oxide

GPE

Gel Polymer Electrolyte

IHP

Inner Helmholtz Plane

IG

ionogel

IG1

Ionogel made of PVDF-HFP and Pyr14TFSI in a 1:4 ratio

IG2

Ionogel made of PVDF-HFP, Pyr14TFSI and SiO2 in a 1:4 ratio

IG3

Ionogel made of PVDF-HFP, Pyr14TFSI and SiO2 in a 1:5 ratio

IG4

Ionogel made of PVDF-HFP, Pyr14TFSI and GO in a 1:4 ratio

IG5

Ionogel made of PVDF-HFP, Pyr14TFSI and GO in a 1:4 ratio

IL

ionic liquid

IL+GO

Solution composed of Pyr14TFSI as the ionic liquid and GO as nanoparticles

IL+SiO2

Solution composed of Pyr14TFSI as the ionic liquid and SiO2 as nanoparticles

IoT

Internet of Things

IP

Immersion Precipitation

Kg

Kilogram

NP

Nanoparticle

OHP

Outer Helmholtz Plane

OCV

Open Circuit Voltage

PEIS

Potentiostatic Electrochemical Impedance Spectroscop

PENG

Piezoelectric Nanogenerator

PIL

Protic Ionic Liquid

PVDF

poly(vinylidene fluoride)

PVDF-HFP

Poly(vinylidene fluoride-co-hexafluoropropylene)

Pyr14TFSI

N-butyl-N-methyl pyrrolidinium bis(trifluoromethanesulfonyl)imide

S

Series of Coin Cell made using IG3 as electrolyte

SC

Supercapacitor

SCPC

Self Charging Power Cell

SCSPC

Self Charging Supercapacitor Power Cell

TGA

Thermo Gravimetric Analysis

TIPS

Thermally Induced Phase Separation

V

Volt

VdW

Van der Waals

W

Watt

Chapter 1

Introduction

With the advent of the new green revolution and the rapid expansion of the Internet of Things (IoT), the demand for reliable energy storage devices has become increasingly crucial. Among various energy storage technologies, supercapacitors (SCs) have garnered significant research interest due to their high power density, rapid charge/discharge cycles, wide operating voltage window, and broad working temperature range.

Despite these advantages, SCs face challenges such as low energy density and gradual voltage loss over time. However, ongoing research is yielding promising advancements, paving the way for next generation SCs suitable for applications in portable electronics, satellite systems, and medical instrumentation.

As one of the key components of a supercapacitor, the choice of the electrolyte plays a fundamental role in determining device performance. Consequently, recent studies have focused on the development of novel electrolytes in various forms to enhance SC efficiency.

This thesis explores the synthesis and characterization of a new class of solid ionogel electrolytes, employing PVDF-HFP as the polymer matrix and $Pyr_{14}TFSI$ as the ionic liquid. Furthermore, the effect of incorporating silica and graphene oxide nanoparticles into the ionogel system will be examined, with a particular focus on their impact on the electrolyte's mechanical, thermal, and electrochemical properties. Finally, the implementation of these advanced electrolytes in a supercapacitor device will be discussed.

1.1 What is a supercapacitor?

There are two primary types of devices used for electrical energy storage: batteries and supercapacitors (SCs).

In batteries, chemical energy is converted into electrical energy through Faradaic

oxidation and reduction reactions occurring at the two electrodes. This process relies on the movement of ions between the anode and cathode, which often results in irreversible chemical changes over time, ultimately limiting the battery's lifespan and recharge cycles.

In contrast, supercapacitors store energy through a non-Faradaic process, meaning no chemical reactions take place. Instead, electrical energy is stored via the accumulation of positive and negative charges on the electrode surfaces, similar to a conventional capacitor. Because no compositional changes occur in the electrode materials, SCs theoretically offer unlimited cycle life and high power density.

However, SCs typically suffer from lower energy density and limited charge storage capacity compared to batteries. Despite this drawback, their high recyclability and fast charge/discharge capabilities make them attractive for various applications [1][2].

In Figure 1.1, a schematic comparison of batteries and supercapacitors is presented, highlighting their fundamental differences.

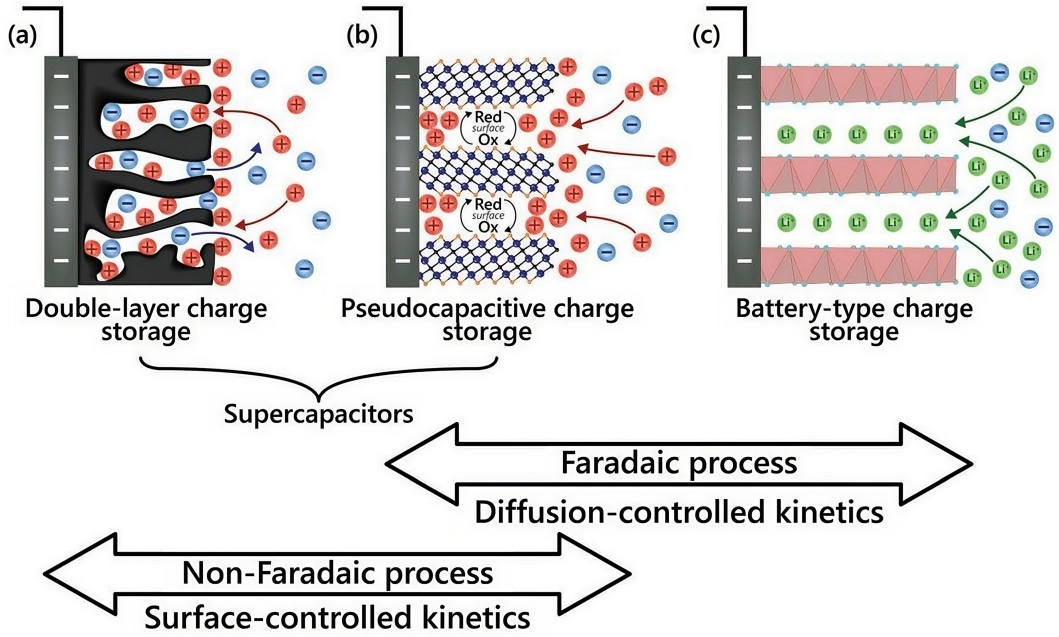

Figure 1.1: Types of electrochemical devices: (a) supercapacitor based on the electrical double layer, (b) supercapacitor based of pseudocapacitance and (c) battery [1].

In a non-Faradaic system, charge accumulation occurs electrostatically when positive and negative charges form at two separate interfaces, similar to a capacitive behavior. Electrochemical capacitors operate based on two primary charge storage mechanisms. Electrical Double Layer (EDL) Capacitance, a non-Faradaic process

occurring at the electrode/electrolyte interface and pseudocapacitance, a Faradaic process involving surface redox reactions that contribute to charge storage.

The electrical double layer (EDL) phenomenon was first introduced by Helmholtz, who described it as two layers of opposite charges separated by an atomic scale distance, resembling a traditional parallel plate capacitor. Initially, the Helmholtz model treated EDL as a 2D phenomenon, useful in explaining colloidal interfaces. Later, Gouy and Chapman refined this theory by introducing the diffuse layer model, where counterions in solution form a gradual charge distribution rather than a rigid layer. This approach considered thermal motion and ion concentration effects. Subsequently, Stern further improved the model by incorporating the finite size of ions, setting geometrical constraints on the layers. In this refined model, the electrical double layer was represented as two capacitors in series, one describing the compact double layer as Helmoltz intended (C_h) and the other describing the diffuse region of the double layer (C_{diff}) obtaining the total capacitance of the double layer (C_{dl}) following Equation 1.1.

$$\frac{1}{C_{\mathrm{dl}}} = \frac{1}{C_{\mathrm{h}}} + \frac{1}{C_{\mathrm{diff}}} \tag{1.1}$$

This model provides a more accurate representation of electrode-electrolyte interactions, improving our understanding of supercapacitor behavior. In Figure 1.2, the three models discussed for the electrical double layer are visualized.

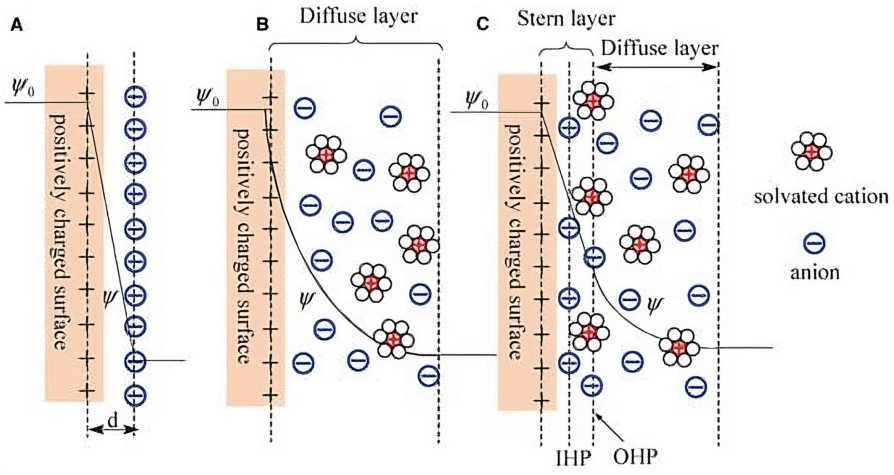

Figure 1.2: Schematic representation of the EDL using the Helmholtz, Gouy-Chapman, and Stern models. IHP denotes the inner Helmholtz plane while OHP refers to the outer Helmholtz plane [3].

In a supercapacitor, it is crucial to recognize that two electrical double layers form at the two oppositely charged electrodes, making it a "two electrode, two

interface system". While the properties of each interface can be studied individually, the overall electrochemical behavior of the device must be analyzed as a whole to accurately understand its performance [2].

As mentioned earlier, pseudocapacitance arises from Faradaic reactions occurring at the electrode surface or within oxide films. Unlike electrical double layer capacitors (EDLCs), where charge is stored electrostatically, pseudocapacitive storage involves charge transfer across the double layer, similar to batteries. However, this process depends on the thermodynamic properties of the system. The term pseudocapacitance is used because the mechanism differs from pure double layer capacitance [4]. These two phenomena are not entirely independent, beacuse studies have shown that 1–5% of the capacitance in some EDLCs is actually pseudocapacitive, while in Faradaic systems, 5–10% of the total capacitance comes from double layer effects [2].

Energy density and power density are two key parameters in the design of electrochemical devices. Energy density refers to the amount of energy a device can store per unit of mass or volume, representing the total energy available for use. It is typically measured in watt hours per kilogram (Wh/kg). In contrast, power density indicates how quickly energy can be delivered per unit of mass or volume, reflecting the rate of energy transfer. It is expressed in watts per kilogram (W/kg).

A device with high energy density can operate for longer before needing a recharge, while high power density allows for rapid energy delivery. Ideally, both properties would be maximized, but in practice, a trade off exists: supercapacitors (SCs) are known for their high power density but relatively low energy density, whereas batteries offer high energy density but lower power density.

The relationship between these two properties is often visualized in a Ragone plot, where specific energy is plotted on the x-axis and specific power on the y-axis, both on a logarithmic scale, as seen in Figure 1.3. These plots typically show a hooked shape, as high power densities are generally associated with lower energy densities. This trend arises from electrode polarization at high discharge rates, when an electrochemical device supplies higher power, the cell voltage drops, reducing energy density, while higher current densities are required [2].

A supercapacitor consists of two electrodes, a binder, a separator, an electrolyte, and a current collector.

In a supercapacitor cell, the electrochemical reaction kinetics are governed by the electrode/electrolyte interface and depend on factors such as the electrode material, surface microstructure, and surface chemistry. For a material to be suitable as an electrode, it must exhibit high electrical conductivity for efficient charge transfer, chemical and electrochemical stability to ensure long term performance, rapid electron transfer to facilitate fast charge/discharge cycles, and reproducibility to maintain consistent electrical, microstructural, and chemical properties across different electrodes.

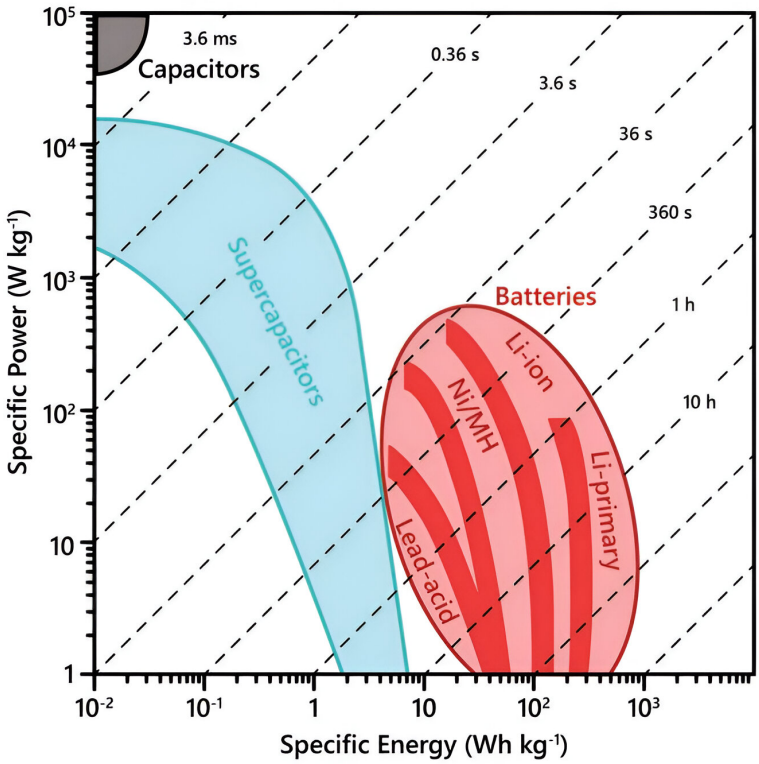

Figure 1.3: Examples of Ragone plots for various electrochemical devices [1].

Before use, electrodes often undergo pretreatment to enhance their performance and achieve an "active" state, characterized by low background current and fast electron transfer rates. Common pretreatment methods include mechanical polishing to remove surface irregularities, vacuum heat treatment to eliminate contaminants and stabilize the surface, electrochemical polarization to optimize charge storage properties, and laser based plasma treatments to modify surface characteristics at the nanoscale.

Another critical aspect of electrode preparation is surface cleanliness. Contaminants can introduce side reactions, unexpected electrochemical behavior, or even alter the electrode's properties, as seen in air oxidation processes [5].

The most widely used electrode material in supercapacitors is carbon, owing to its diverse microstructures, including graphite, glassy carbon, carbon fibers, amorphous carbon, carbon nanotubes, and diamond like carbon. This versatility allows for tunable electrochemical properties and surface chemistry, making carbon electrodes suitable for a wide range of applications. Another common class of electrodes is metal based, particularly gold and platinum, which are valued for their fast electron transfer kinetics and wide anodic potential window. However,

for metal electrodes, surface control is critical to prevent oxide formation, which can alter reaction kinetics and mechanisms in certain systems.

The choice of electrode material defines the working principle of a supercapacitor. Materials such as graphene, carbon nanotubes, and activated carbon exhibit electrical double layer capacitance (EDLC), where charge is stored electrostatically at the electrode/electrolyte interface. In contrast, conducting polymers and metal oxides exhibit pseudocapacitance, which involves Faradaic charge transfer reactions at the surface. Supercapacitors that utilize such materials are classified as pseudocapacitors [2].

Aside from the electrodes, the electrolyte plays a crucial role in supercapacitor performance. The efficiency of charge transfer and accumulation at the electrode/-electrolyte interface directly impacts the device's capacitance, power density, and energy storage capabilities. An ideal electrolyte should possess high ionic conductivity to facilitate rapid charge transport, a broad electrochemical stability window to enable higher operating voltages, and a high density of free ions for efficient charge storage. Additionally, it should exhibit low toxicity for environmental and safety considerations, as well as good thermal and electrochemical stability for long term durability. A detailed discussion of electrolytes will follow in the next section.

1.2 Electrolytes: a quick overview

As previously mentioned, the electrolyte is a crucial component of a supercapacitor, facilitating ion transport between the positive and negative electrodes during charge and discharge cycles. In addition to enabling ion movement, electrolytes usually act as a separator, preventing short circuits between the electrodes [6]. High ionic conductivity is essential for the rapid formation of the electrical double layer, while the electrolyte's electrochemical stability potential window (ESPW) determines the maximum operating voltage of the supercapacitor. The selection of an electrolyte with low equivalent series resistance (ESR) supports fast charging and discharging, enhancing the device's power density. Furthermore, electrolytes influence the supercapacitor's operating temperature range and long term stability by reducing electrode degradation over repeated cycles. Figure 1.4 provides an overview of the key properties that can be optimized in an electrolyte while Figure 1.5 provides a visual overview of the different types of electrolytes commonly used in electrochemical devices.

Aqueous electrolytes are primarily used for their high ionic conductivity and cost effectiveness. However, their application in commercial electrochemical products is limited by a narrow electrochemical stability potential window (ESPW). These electrolytes are classified into acidic, alkaline, and neutral, based on the ions present in the solution, with sulfuric acid, potassium hydroxide, and sodium sulfate

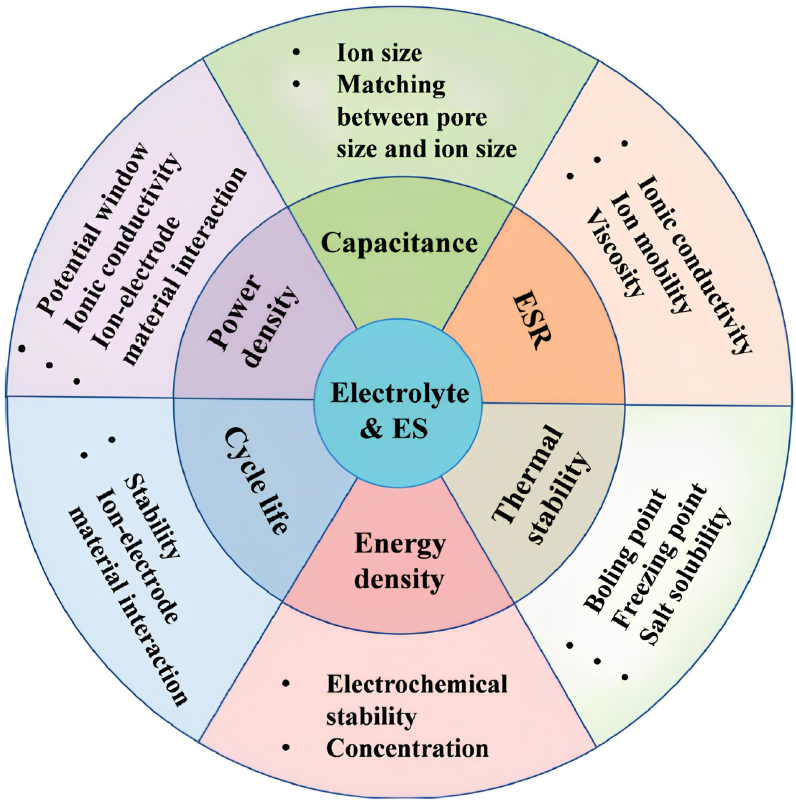

Figure 1.4: Properties required for a good electrolyte [7].

being the most commonly used [8]. Acidic electrolytes exhibit high capacitance, particularly when combined with carbon based electrodes, but their corrosive nature restricts material compatibility and long term stability [7]. Alkaline electrolytes are more suitable for pseudocapacitors and hybrid supercapacitors, yet they share the same drawbacks as their acidic counterparts. Neutral aqueous electrolytes offer the advantage of enhanced safety and non corrosive behavior, but at the cost of lower ionic conductivity. Recent studies have focused on expanding the ESPW of aqueous electrolytes by incorporating salts, with lithium bis(trifluoromethanesulfonyl)imide (LiTFSI) emerging as a common choice [9].

Organic electrolytes typically consist of an organic solvent, most commonly acetonitrile or propylene carbonate, combined with an electrolyte salt, such as tetraalkylammonium salts [7]. Compared to their aqueous counterparts, organic electrolytes are more expensive, exhibit lower specific capacitance, and have reduced ionic conductivity [10]. Their higher viscosity hinders ion transport, and their components are often toxic and highly flammable. Additionally, they require extensive purification processes and have a relatively low maximum operating

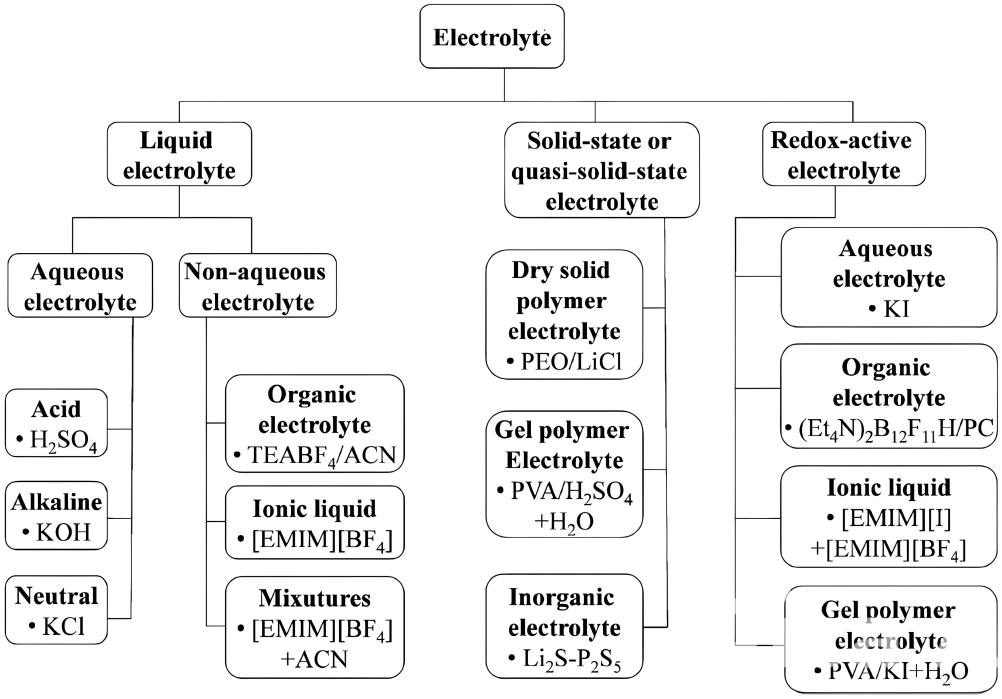

Figure 1.5: Classification of electrolytes [7].

temperature, usually below 70 °C. Despite these drawbacks, organic electrolytes offer a wider potential window, higher energy density, and lower corrosion rates, making them the preferred choice for commercial supercapacitors over aqueous electrolytes. Recent research efforts have been directed toward developing less toxic organic electrolytes and optimizing solvent/salt combinations to improve performance and safety.

Ionic liquids (ILs) have been extensively studied as electrolyte materials due to their unique properties as ionic salts. Unlike aqueous and organic electrolytes, ILs consist entirely of ions, providing significant advantages in electrochemical applications. These electrolytes are typically composed of cations such as imidazolium or pyrrolidinium and anions like tetrafluoroborate or bis(trifluoromethylsulfonyl)imide. They offer a broad electrochemical stability window, with ionic conductivity comparable to that of organic electrolytes. Additionally, ILs exhibit high thermal stability, often exceeding 300 °C, while maintaining a liquid state even at low temperatures. Their low volatility and non flammable nature make them particularly suitable for high voltage and high temperature applications. However, their high viscosity can hinder ion diffusion, and their complex synthesis and purification processes contribute to elevated costs [7]. To address these challenges, recent research has focused on reducing viscosity by blending ILs with organic solvents or polymers.

Solid state electrolytes are cost effective, non toxic materials that offer a wide electrochemical stability window, strong mechanical properties, and high conductivity. They also enhance device reliability by preventing leakage, reducing packaging costs. This class of electrolytes is divided into polymer electrolytes, gel electrolytes, and inorganic solid state electrolytes.

Solid state polymer electrolytes are typically composed of polyvinyl alcohol (PVA), polyethylene oxide (PEO), or polyacrylonitrile (PAN). These materials are flexible and easily processed into thin films, but they exhibit lower conductivity than liquid electrolytes.

Gel polymer electrolytes (GPEs) improve upon this limitation by offering higher ionic conductivity and better interfacial contact with electrodes. GPEs consist of a polymer matrix, a plasticizing solvent, and an electrolyte salt [11]. The polymer matrix is usually made from PEO, PAN, or poly(vinylidene fluoride) (PVDF) and its copolymers, while common plasticizers include propylene carbonate, ethylene carbonate, and tetrahydrofuran. However, due to their liquid content, GPEs have limited mechanical strength and reduced thermal stability.

Inorganic solid state electrolytes, on the other hand, provide excellent mechanical strength along with high thermal and electrochemical stability. However, they lack flexibility and bendability. Below their melting point, they exhibit good lithium ion conductivity, making them suitable for high performance applications. The most common inorganic electrolytes are ceramic based materials such as lithium lanthanum zirconate (LLZO) and sodium superionic conductors (NASICON).

IL electrolytes and gel polymer electrolytes will be explored in greater detail in their respective sections, as they represent a key focus of this thesis.

Another category of electrolytes consists of those containing redox active species dispersed in an aqueous medium. These electrolytes store energy through Faradaic reactions occurring at the electrode interface. They offer excellent interfacial contact with electrodes, superior ionic conductivity compared to solid electrolytes, and fast ion transport capabilities, thereby enhancing energy density without compromising power density. However, their main drawbacks include the limited solubility of redox species in certain solvents and the potential for self degradation over time, which reduces the cycle life of the device.

Current research in this field has focused on iodide and bromide based redox species due to their advantageous pseudocapacitive effects and efficient Faradaic charge transfer. Sulfide based redox species have also gained interest for their cost effectiveness, high solubility in aqueous solutions, and non toxic nature [12].

Table 1.1 provides a quick comparison of the properties of various types of electrolytes.

Type of electrolyte	ESPW	Ionic Conductivity	T Stability	Cost
Acqueous	1.0-1.3 V	0.1-0.8 S/cm	0°C to 80°C	Low
Organic	2.5-2.8 V	0.01-0.1 S/cm	-40°C to 70°C	Medium
Ionic Liquid	3.5-4.0 V	0.01-0.1 S/cm	>300°C	High
Solid-state	1.0-3.0 V	10^{-3} S/cm	-20°C to 200°C	Medium
Redox-active	1.0-3.0 V	Variable	20°C to 80°C	Variable

Table 1.1: Comparison of the characteristics of various types of electrolytes [7].

1.3 An in-depth analysis of IL electrolytes

As previously mentioned, ILs are a promising option as electrolytes for supercapacitor applications, particularly due to the virtually unlimited combinations of anions and cations that can be used to tailor their properties. However, many of these combinations are challenging to synthesize, costly, and often impractical for widespread use due to their high viscosity [13]. The selection of anions and cations not only influences the physical properties of the electrolyte but also affects the structure of the electrical double layer at the electrode interfaces. This makes the choice of electrode material another critical factor in the design of an efficient supercapacitor [14][15]. Additionally, the capacitance of the device is significantly impacted by the ion size within the electrolyte, further emphasizing the importance of selecting an optimal anion/cation pair [16].

ILs are categorized into four types based on their cation composition: alkylammonium-, dialkylimidazolium-, phosphonium-, and N-alkylpyridinium-based ILs [17], as illustrated in Figure 1.6.

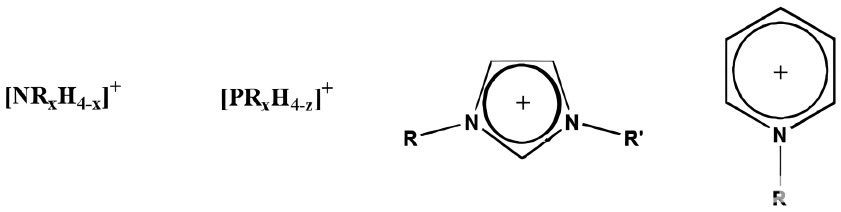

Figure 1.6: Structures of the most common cations for IL, from left to right: alkylammonium-, phosphonium-, dialkylimidazolium- and N-alkylpyridinium cations [17]

The first IL ever synthesized was ethanolammonium nitrate (EOAN), an ammonium based IL. This category has been widely used in electrochemical applications due to its excellent cathodic stability, low melting point, and low viscosity [18]. Imidazolium based ILs have gained significant attention for their stability under

oxidative and reductive conditions, low viscosity, and ease of synthesis [19][20]. However, their use under basic conditions is limited due to unexpected side reactions caused by the deprotonation of the imidazolium cation [21]. Pyridinium based ILs have been employed in reactions such as Friedel Crafts and Grignard, as well as in electrochemical devices, owing to their overall good stability. The most recently studied category, phosphonium based ILs, exhibit superior thermal stability, withstanding temperatures up to 400°C. They are primarily used as catalysts and in CO_2 capture applications but are susceptible to reactions with small bases [22].

ILs can also be classified into protic ILs (PILs) and aprotic ILs (APILs) based on their chemical structure and the presence or absence of transferable protons, as illustrated in Figure 1.7. PILs contain protons that can participate in hydrogen bonding or acid/base reactions, making them widely used in biological systems, chromatography, and as proton conducting electrolytes for polymer membrane fuel cells. In contrast, APILs lack transferable protons, and their cations are typically bulky, resulting in higher viscosity compared to PILs. Although APILs are more expensive and complex to synthesize, their lack of hydrogen bonding, which can hinder conductivity, and their wide electrochemical stability potential window (ESPW) make them ideal for high voltage applications such as supercapacitors.

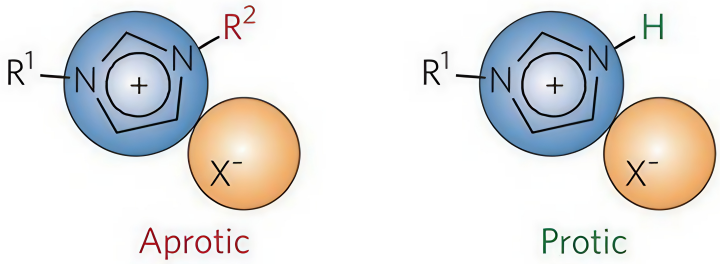

Figure 1.7: Difference between protic and aprotic ILs [7].

One approach to enhancing the properties of IL electrolytes involves mixing two ILs that share the same cation but have different anions. This method creates a thin double layer at the electrode/electrolyte interface, maximizing contact area due to the disruptive effect of larger anions over smaller ones. Alternatively, eutectic mixtures of protic ILs can be formed by combining different cations with the same anion. This prevents the formation of an ordered lattice at the interface, as the varying molecular structures of the cations disrupt regular packing [23][24].

Another strategy is to blend ILs with organic solvents, reducing viscosity and increasing conductivity, albeit at the cost of a narrower potential window. A similar effect can be achieved by introducing ionic salts into ILs, which alters the ionic

arrangement within the electrolyte and enhances capacitive performance. Additionally, incorporating electroactive species into ILs can boost device capacitance by facilitating faradaic reactions at the electrode interfaces [25][26].

ILs can also be dispersed in aqueous solutions as ionic salts, where their electroactive ions contribute to charge storage. In aqueous electrolytes, ion size plays a crucial role because smaller ions lead to stronger polarization and reduced supercapacitor performance, while larger ions are generally more suitable [27][28]. Moreover, the typically high cost of ILs is less of a concern in these electrolytes, as only a small amount is required for effective operation.

N-butyl-N-methyl pyrrolidinium bis(trifluoromethanesulfonyl)imide ($Pyr_{14}TFSI$) was selected for this thesis due to its availability and strong performance in supercapacitor applications, with an anodic stability window of 5,85 V [29]. $Pyr_{14}TFSI$ exhibits a conductance of 3.2 mS/cm at 40°C, which is relatively lower compared to other ILs such as EMITFSI. This is primarily due to its higher viscosity, measured at 40 mPa·s [30][31]. The molecular structures of the ions comprising $Pyr_{14}TFSI$ are depicted in Figure 1.8.

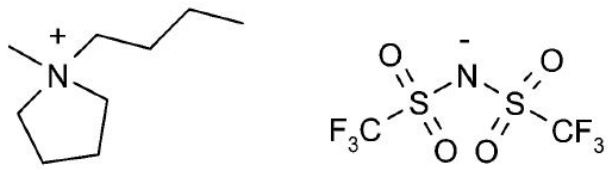

Figure 1.8: Structure of $Pyr_{14}TFSI$ [31].

1.4 Ionogels as electrolytes

The previous section highlighted both the strong advantages and notable drawbacks of IL electrolytes. Perhaps their most significant disadvantage is that, despite their typically high viscosity, ILs remain in a liquid state. This can lead to potential cell leakage, which not only affects device reliability but also limits their practical applications. To address this issue, integrating ILs into solid or quasi solid electrolytes has gained increasing attention in recent research [32]. The most common approach involves immobilizing ILs within a polymer matrix to prevent leakage while preserving ionic mobility, though a slight reduction in ionic conductivity is typically observed [33]. However, the high viscosity of ILs can actually enhance the mechanical properties of gel electrolytes, improving flexibility and bendability when incorporated into a device. Additionally, the presence of ILs in the polymer matrix expands the electrochemical stability window of the electrolyte.

A crucial factor in this approach is the careful selection of a compatible IL and polymer matrix to ensure good ion mobility and maintain high ionic conductivity.

A sub class of these electrolytes is the so called ionogel, a crosslinked polymer network with dispersed ILs, typically resulting in a porous structure. Depending on the nature of the crosslinks, ionogels can be classified as either physically or chemically cross linked. In physically cross linked ionogels, the polymeric network is formed through non covalent interactions such as Van der Waals forces, hydrogen bonding, and electrostatic interactions. In contrast, chemically cross linked ionogels rely on the formation of covalent bonds to create a stable network [34]. Ionogels can be synthesized using various methods, with direct mixing, in situ polymerization/gelation, and solvent exchange being the most commonly employed techniques.

Direct mixing is one of the simplest methods for obtaining ionogels. It involves preparing a solution containing a polymer matrix and an IL, where the ionogel forms through the swelling of the host material. However, ILs and commercially available polymer hosts often have low miscibility. A common solution is to introduce a second solvent, which is later removed after the formation of the crosslinked network [35]. To achieve smooth ionogel films, the solution is typically cast and then processed using spin or blade coating.

In situ polymerization and gelation rely on thermal or UV initiated free radical polymerization, as well as ring opening polymerization, to form the crosslinked network. However, ILs can sometimes interfere with this process, limiting its applicability.

When polymer IL miscibility is poor, the solvent exchange method is an effective alternative. This process begins by mixing the polymer with water or an organic solvent, followed by polymerization or gelation to form the network. The resulting gel is then immersed in the desired IL, and the solvent exchange is achieved by removing the initial solvent [36].

Thanks to the presence of ILs in their matrix, ionogels exhibit exceptional properties such as non volatility, high ionic conductivity, thermal stability, and emerging features like recyclability and self healing. However, their primary drawback lies in their poor mechanical properties, including low toughness, weak strength, and sensitivity to crack propagation [37]. To address these issues, researchers are exploring strategies such as double network structures, nanocomposites, supramolecular interactions, and phase separation within the gel.

Introducing a second polymer network enhances energy dissipation during stretching, as the two networks are not covalently bonded. Under deformation, the dissipative network breaks while the high tensile strength network stretches, preserving the gel's integrity [38]. Additionally, incorporating nanoparticles into the matrix increases polymer entanglement and acts as stress transfer and dissipation centers, improving mechanical stability.

Ionogels also demonstrate strong resistance to extreme temperatures due to the IL component, and modifying the IL structure can further enhance their thermal stability. Their ionic conductivity depends on both the IL and the polymer matrix. The viscosity of the IL is influenced by ion size, with smaller anions and shorter cationic alkyl chains reducing viscosity and thereby improving conductivity. However, ionogels typically exhibit lower ionic conductivity than their pure IL counterparts. Increasing IL content can enhance conductivity but often compromises mechanical strength.

In supercapacitor applications, ionogels have gained traction due to their high electrical conductivity, customizable shapes, broad electrochemical window, and favorable thermal and mechanical properties.

1.4.1 Interfacial interactions in ionogels

The defining characteristic of ionogels is their ability to retain liquid like properties while maintaining a solid structure. They exhibit unique interfacial interactions, with the key types illustrated in Figure 1.9.

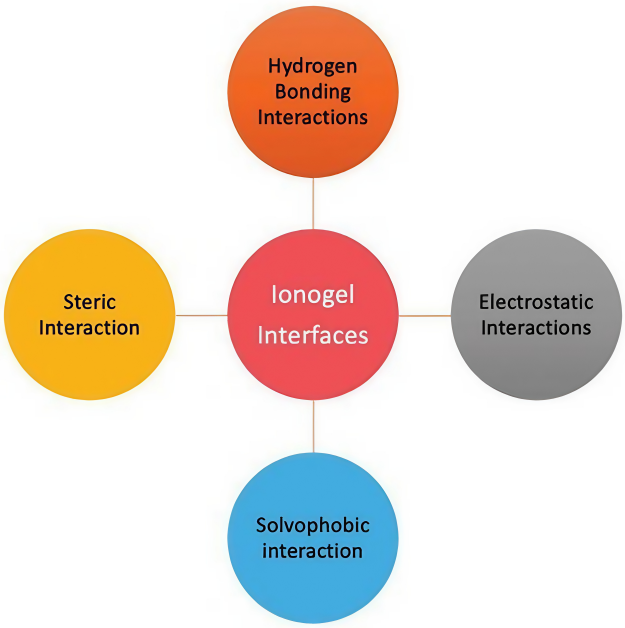

Figure 1.9: Interfacial interactions in Ionogels [39].

Hydrogen bonding, one of the strongest forces acting on ions in an IL, also plays a crucial role in IGs, significantly impacting the system's reaction dynamics [40]. Beyond being the primary non covalent force driving gelation during the

ionogel formation process, hydrogen bonding also enhances mechanical properties by strengthening interactions between the IL and the polymer matrix.

Electrostatic interactions, including Van der Waals (VdW) forces, play a crucial role in determining the thermodynamic properties of an IG. Studies have shown that these interactions between the IL and the polymer matrix enhance ionogel performance by stabilizing the polymer network, allowing for the incorporation of high IL content, and thereby improving ionic conductivity. Additionally, electrostatic interactions contribute to the self standing membrane behavior of ionogels and influence the crystallization kinetics of the polymer due to the local dipole moment between the ILs and the polymer matrix. This results in a higher degree of crystallinity, which reduces ionic conductivity, while also increasing the glass transition temperature, limiting polymer mobility, and further hindering ion transport [41].

Solvophobic interactions play a crucial role in the compatibility of ionogels. Shorter alkyl chains improve the miscibility of ILs with the polymer matrix by enhancing solvophobic interactions [42]. These interactions are also significant in the gelation process of IGs, influencing their structural formation and stability.

As previously mentioned, the properties of ionogels are primarily governed by the ionic liquid content. A higher IL concentration enhances ionic conductivity by introducing additional charge carriers and acting as a plasticizer, softening the polymer backbone and resulting in a sticky electrolyte. This sticky behavior not only improves ionic transport but also enhances electrolyte/electrode contact. Additionally, increasing IL content reduces the polymer's crystallinity, further boosting ionic conductivity. However, this also leads to a decline in the mechanical properties of the ionogel.

1.4.2 PVDF as a ionogel matrix

Poly(vinylidene fluoride) (PVDF) is an odorless, tasteless, and non toxic semicrystalline polymer, composed of approximately 60 wt% fluorine and 3 wt% hydrogen. As an electroactive polymer (EAP), PVDF is widely used in supercapacitor fabrication, serving as a binder, electrolyte, and separator, as illustrated in Figure 1.10. EAPs are known for their ability to undergo large deformations in response to small stimuli, such as electric fields [43].

In a supercapacitor, the binder secures the active material within the electrode, ensuring strong electrical interactions between components. Key factors for an effective binder include adhesion strength, hydrophilicity, non toxicity, and thermal and electrical stability. Additionally, the binder concentration plays a crucial role in electrode fabrication. A well chosen binder minimizes electron transfer resistance at the interface and enhances pseudocapacitive charging. PVDF is widely used as a binder due to its compatibility with nearly all active materials. It is typically combined with a conductive agent, such as carbon black or graphite, to mitigate

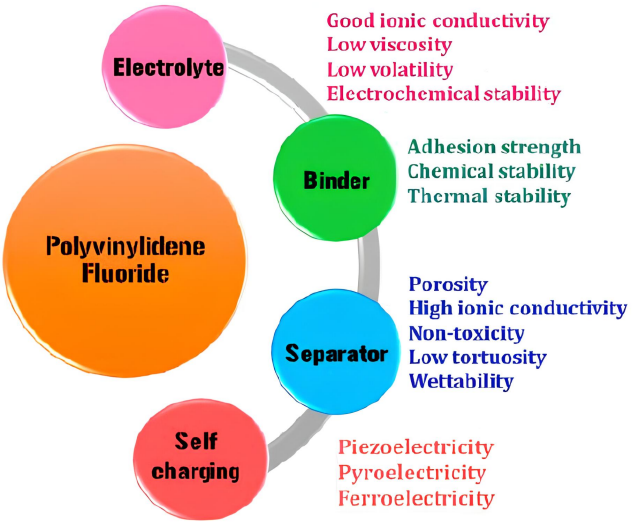

Figure 1.10: Various ways to use PVDF in an electrochemical device [44].

any negative impact on conductivity. When dispersed in a suitable solvent, PVDF forms Van der Waals bonds with the active material, producing more compact and efficient electrodes.

Among the various materials available for electrolytes, PVDF is considered one of the best choices for supercapacitors and nanogenerators due to its strong polar C–F bond and high dielectric constant (ε). Both PVDF and P(VDF-HFP) are commonly used in gel electrolytes to enhance mechanical stability and improve ionic conductivity, ensuring reliable performance even at low scan rates.

As a separator, PVDF prevents direct contact between the electrodes while allowing the free movement of ions from the electrolyte to the electrodes. An ideal separator should be strong yet thin to ensure device durability and must remain stable within the operating potential range. Additionally, it should be chemically resistant to the electrolyte to prevent corrosion. In recent years, polymer based separators have gained popularity due to their adaptability, mechanical and chemical strength, high porosity, wettability, and thermal stability [44].

Unlike other polymers, PVDF is unique in possessing piezoelectric properties, making it highly valuable for energy harvesting and storage applications, such as piezoelectric nanogenerators (PENGs) and self charging power cells (SCPCs). These devices convert mechanical energy into electrical energy and store it within the system. The flexibility of PVDF has inspired research into lightweight and flexible supercapacitors, including self charging supercapacitor power cells (SCSPCs). These devices generate an electric charge under mechanical stress due to the polarization of the PVDF separator and the movement of ions in the electrolyte.

Unlike other crystalline polymers, PVDF exhibits excellent compatibility with other polymers, enabling the fabrication of membranes with tailored properties. Commercially, PVDF is synthesized via emulsion or suspension polymerization using free radical initiators. The polymer chain consists of alternating CH_2 and CF_2 groups, where CH_2 units are referred to as 'tail' and CF_2 units as 'head.' Due to the non regiospecific nature of polymerization, PVDF may contain reversed monomer sequences, such as head-to-head and tail-to-tail linkages. Structural variations in PVDF can be observed in Figure 1.11 and Figure 1.12. The crystallization behavior of PVDF is influenced by factors such as molecular weight, molecular weight distribution, thermal history, and cooling rate, with its degree of crystallinity typically ranging from 35% to 70%.

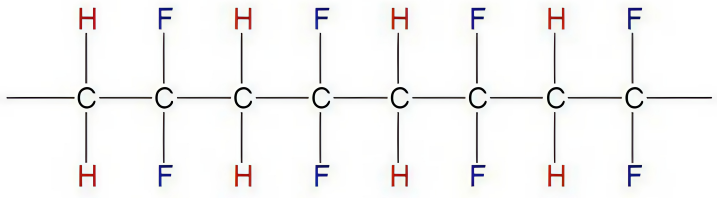

Figure 1.11: Classic structure of a PVDF chain [45].

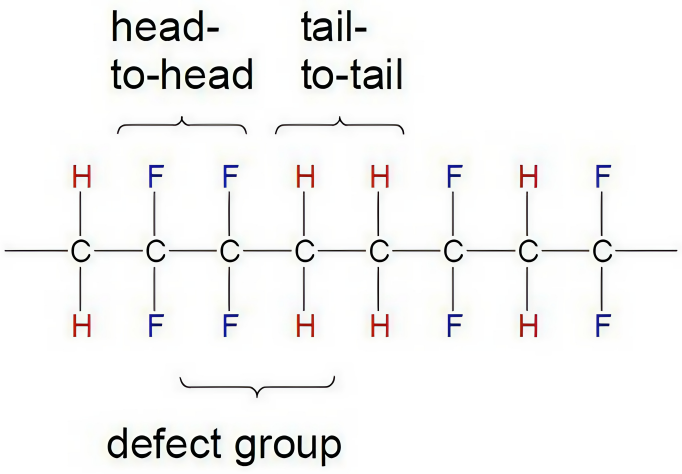

Figure 1.12: PVDF chain with head-to-head and tail-to-tail structure due to non-regiospecificity [45].

PVDF chains crystallize into four distinct phases: alpha, beta, gamma, and delta, with alpha and beta being the most prevalent. The alpha phase, which forms through polymer crystallization from the melt, is the most common and adopts a

distorted trans-gauche-trans-gauche' (TGTG') conformation. It is the non polar form of PVDF. Conversely, the beta phase is polar and typically emerges when the polymer backbone undergoes stretching, straining, or quenching. This phase exhibits a distorted, planar zigzag, all trans conformation and is particularly valued for its piezoelectric properties [45]. The structural differences between the alpha and beta phases are illustrated in Figure 1.13. The primary techniques employed in the literature to determine the degree of different crystal forms in PVDF include infrared (IR) spectroscopy, Fourier transform infrared (FTIR) spectroscopy, and X-ray diffraction (XRD) spectroscopy.

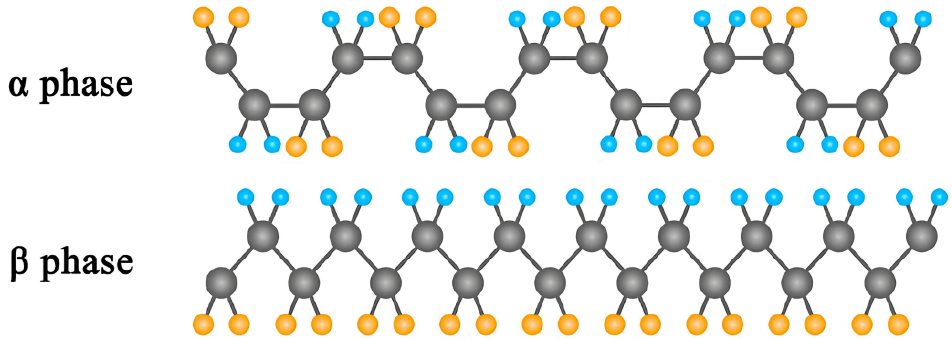

Figure 1.13: Difference of alpha and beta phase conformations [44].

As mentioned earlier, PVDF exhibits excellent thermal stability due to the high electronegativity of fluorine atoms and the strong bond dissociation energy of the C-F bond. It has a glass transition temperature of -40 °C and a melting temperature of 140 °C. PVDF remains thermally stable up to 375 °C, with its degradation mechanism primarily involving the loss of hydrogen fluoride (HF). This process triggers chemical reactions such as polymer chain cross linking and the formation of carbon-carbon double bonds.

In addition to its thermal stability, PVDF demonstrates remarkable chemical resistance, withstanding exposure to halogens, oxidants, aliphatic and aromatic solvents, and inorganic acids. However, strong bases, ethers, and ketones can degrade PVDF membranes. Notably, sodium hydroxide solutions attack the alpha phase, causing discoloration. Changes in temperature and pressure can further accelerate the degradation process [43].

Copolymers of PVDF, such as poly(vinylidene fluoride-co-hexafluoropropylene) (P(VDF-HFP)), have been widely used in supercapacitors, sensors, and nanogenerators. The introduction of hexafluoropropylene (HFP) disrupts the crystallinity of the polymer matrix due to the presence of CH_3 groups in the HFP monomer, leading to a lower melting point. However, this modification results in a more homogeneous morphology, with a uniform distribution of the crystalline PVDF

phase and the amorphous co-monomer.

The increased amorphous phase in P(VDF-HFP) improves chain mobility and flexibility while enhancing ionic conductivity and hydrophobicity due to the higher fluorine content. These properties make P(VDF-HFP) particularly suitable for applications requiring both mechanical adaptability and efficient ion transport. The structure of PVDF-HFP is shown in Figure 1.14.

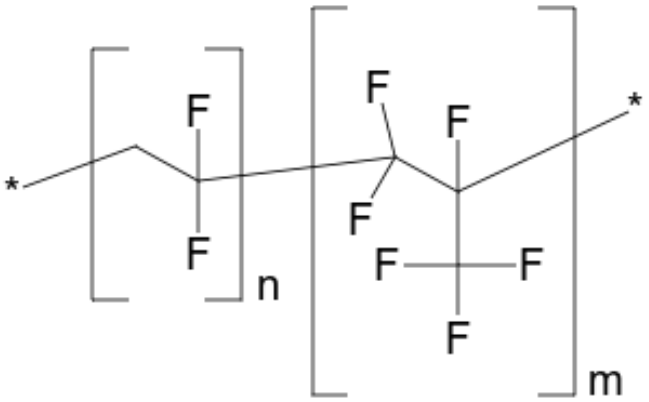

Figure 1.14: Structure of PVDF-HFP.

PVDF membranes can be produced using various methods, including phase inversion with inorganic particles as fillers or additives, sintering, and track etching [43]. Among these, the phase inversion method is the most widely used due to its simplicity, flexibility, and cost effectiveness. This process involves the transition of a homogeneous polymer solution into a solid membrane through thermally induced phase separation (TIPS) or immersion precipitation (IP).

A crucial factor in achieving high performance membranes is the selection of a suitable solvent, as it ensures uniform polymer distribution and prevents aggregation, which can compromise membrane properties.

Immersion precipitation (IP) is the primary technique for PVDF membrane fabrication. This process involves immersing a cast polymer solution into a coagulation bath containing a non solvent, inducing phase separation. However, the semi crystalline nature of PVDF complicates the process, prompting researchers to optimize membrane preparation. Commonly used high boiling point solvents include N,N-dimethylacetamide (DMF) and dimethyl sulfoxide (DMSO), while

low boiling point solvents such as acetone and tetrahydrofuran (THF) are also employed. Membrane formation in the coagulation bath is governed by two mechanisms: liquid-liquid demixing and crystallization. Water is the most frequently used non solvent, typically leading to finger like voids due to rapid coagulation. Adjusting the solvent composition or lowering the water bath temperature can modify the membrane structure, resulting in a more sponge like morphology.

The thermally induced phase separation (TIPS) method involves dissolving PVDF in a high boiling point diluent at elevated temperatures, followed by casting and controlled cooling to induce phase separation. The choice of diluent plays a crucial role in determining the final membrane characteristics. Common diluents include dibutyl phthalate (DBP), dioctyl sebacate (DOS), and dioctyl adipate (DOA), each influencing the crystallization temperature of PVDF. Depending on the system's miscibility, phase separation in TIPS can occur through solid-liquid (S-L) or liquid-liquid (L-L) mechanisms.

Two additional techniques for fabricating PVDF membranes are sintering and track etching. In the sintering process, PVDF powder is compressed and heated, resulting in either porous or dense membranes, depending on the processing conditions. Track etching, on the other hand, involves irradiating a polymer film with metal ions, followed by etching in an acid or alkaline bath to create cylindrical pores, with their size controlled by process parameters.

Recently, electrospinning has emerged as a highly effective method for PVDF separator fabrication. Compared to phase inversion or solvent evaporation, electrospun PVDF microfibers offer several advantages, including high porosity, a large surface area, improved electrolyte uptake, enhanced ionic conductivity, and reduced interfacial resistance [44].

The piezoelectric properties of PVDF arise from its beta phase, which also exhibits pyroelectric and ferroelectric characteristics. In semi crystalline PVDF, the piezoelectric effect originates from induced dipole polarization. Maximizing these properties requires increasing the beta phase content, which can be achieved through quenching and annealing, mechanical stretching, or the incorporation of nanofillers. These nanofillers facilitate the alpha to beta phase transition by creating favorable nucleation sites [45].

1.5 Nanoparticles in ionogels and their effects

While ionogels offer advantages such as flexibility and electrode compatibility, their ionic conductivity must be significantly improved for efficient supercapacitor applications. One solution is the incorporation of nanofillers into the polymer matrix, which enhances ionic conductivity, mechanical strength, and electrochemical stability, making them more suitable for high performance devices.

As previously mentioned, incorporating nanoparticles (NPs) into the polymer matrix enhances the performance of ionogels, particularly their thermal and mechanical properties. NPs can also mitigate the negative effects of high IL loading, maintaining flexibility while reducing fragility. However, if not carefully managed, NPs may coagulate due to strong cohesive interactions [46]. Additionally, the ceramic/polymer interface plays a crucial role in determining the properties of composite electrolytes.

Inorganic fillers in ionogels can be classified as either passive or active, depending on their influence on ion transport. Passive inorganic fillers enhance ionic conductivity by disrupting polymer crystallinity, reducing the matrix's glass transition temperature, and shortening polymer chains, all of which improve ion mobility. Additionally, electrostatic interactions between the nanoparticle surfaces and ions create new pathways for ion transport. Active fillers, on the other hand, generate multiple ion transport pathways in ceramic polymer composites, including intrapolymer transport, intraceramic transport, and interfacial polymer/ceramic transport, depending on the specific interactions within the composite [47].

1.5.1 Types of nanoparticles used in ionogels

The most commonly used passive fillers in composite electrolytes include aluminum oxide (Al_2O_3), silica (SiO_2), titanium oxide (TiO_2), and zinc oxide (ZnO), while active fillers typically consist of perovskite structured lithium lanthanum titanium oxide (LLTO), NASICON-type materials, and sulfides [48].

The dispersion of ceramics in a nanofiller can take various forms: 0D (nanoparticles or powders), 1D (nanowires or nanotubes), 2D (nanosheets), and 3D (network membranes). 0D nanoparticles, as mentioned earlier, can suppress polymer crystallization and enhance ion transport, but excessive loading often leads to particle aggregation. To overcome this, 1D nanowires and nanotubes have been explored as alternatives, as they allow higher filler content and provide continuous ion transport pathways. These nanofillers can be either randomly dispersed or aligned, depending on the fabrication method. Additionally, 3D ceramic nanofiber networks can serve as a scaffold, into which a polymer is infiltrated to form a 3D ceramic composite electrolyte. Meanwhile, 2D nanosheets offer an ultrathin structure with a high surface area for interactions, but their inherent anisotropy and chemical functionality limit their widespread application [49].

Carbon based nanofillers have also been widely studied due to the exceptional properties of carbon materials. Researchers have discovered that certain ILs can chemically modify and optimally disperse carbon nanotubes (CNTs) within the polymer matrix, leading to enhanced mechanical and thermal properties [50].

In addition, metals such as silver, gold, copper, and platinum have been explored as nanofillers due to their unique physical and chemical characteristics. These

metal fillers can be either uniformly dispersed within the material or confined to the surface, providing some degree of flexibility. However, their high tendency to agglomerate and weak chemical interactions with polymers pose significant challenges. This issue can be partially mitigated by selecting a suitable IL to improve dispersion and compatibility [51].

In this thesis study, the chosen nanoparticles are silica and graphene oxide. Research has demonstrated that incorporating SiO_2 into a solution of PVDF and EMITFSI enhances ionic conductivity by reducing crystallinity, as shown in Figure 1.15. The silica NPs increase the free volume within the three dimensional polymer network, facilitating faster ion movement. Additionally, the resulting membrane exhibits improved mechanical and thermal properties compared to the NP free counterpart, minimizing the risk of leakage in high temperature applications [52].

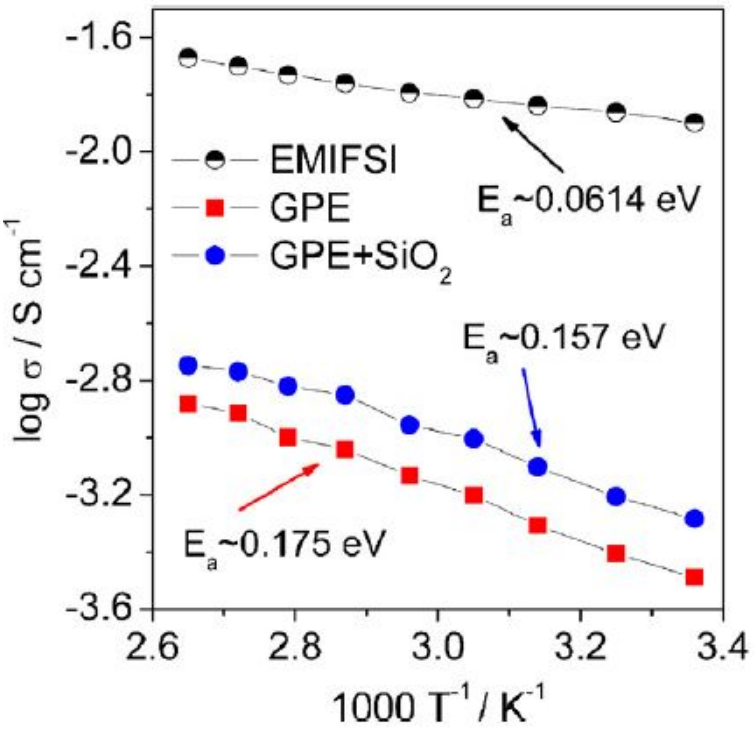

Figure 1.15: Conductance variation shown in the study [52].

Graphene oxide (GO) has been incorporated into ionogels containing PVDF-HFP and $EMIMBF_4$ to enhance membrane properties. Studies have shown that the addition of GO significantly increases the ionic conductivity of the ionogel, even surpassing the conductance of pure $EMIMBF_4$. Various concentrations of GO

and IL were investigated, as illustrated in Figure 1.16. While a higher IL content improved the ionogel's conductivity, exceeding the optimal GO concentration of 1 wt% relative to the polymer led to a decline in conductive properties due to nanoparticle agglomeration [53].

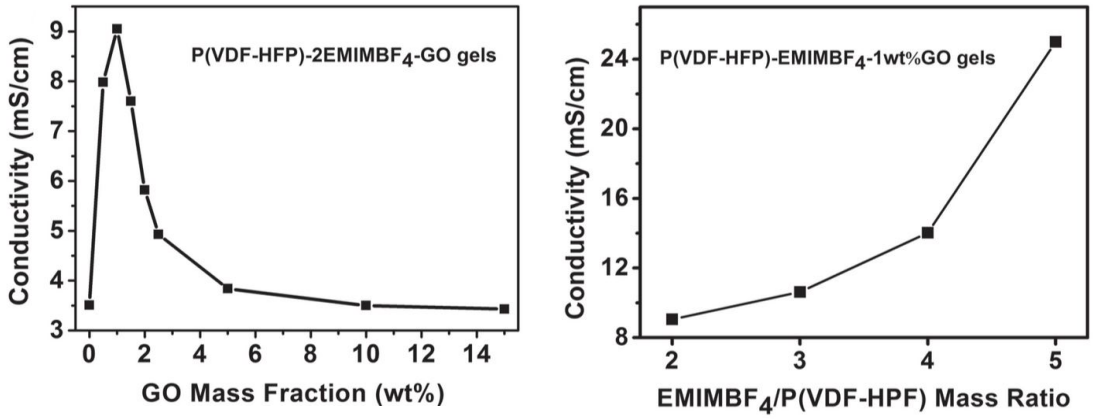

Figure 1.16: Conductance study: on the left, different content of GO in the solution; on the right, different IL content in the solution [53].

Chapter 2

Experimental

2.1 Techniques and methods used in this thesis work

2.1.1 TGA

The Thermo Gravimetric Analysis (TGA) is a technique used to analyze the thermal behavior of a sample by monitoring its weight loss as the temperature increases at a controlled rate.

The sample is placed in an inert alumina crucible, which is positioned on a precision scale inside a furnace. The atmosphere within the chamber can be adjusted depending on the gas used, typically nitrogen for an inert environment or oxygen for an oxidizing one. The sample's degradation behavior is influenced by the type of atmosphere present. The degradation products can be carried away by the gas flux to other instruments, such as a gas chromatograph (GC), mass spectrometer (MS), or infrared spectrometer (FT-IR), for further analysis.

The output of a TGA analysis is typically a plot with temperature on the x-axis and mass percentage on the y-axis. The mass loss is represented by changes in the slope of the curve, creating a characteristic step like pattern. To better interpret weight loss behavior, it is common practice to use the derivative of the curve (DTGA), where peaks indicate the temperatures at which the maximum degradation rates occur. Any remaining mass at the end of the analysis typically consists of inert or non degradable components in the sample.

The instrument used in this thesis work, as shown in Figure 2.1, is the NETZSCH TG 209 F1 Libra.

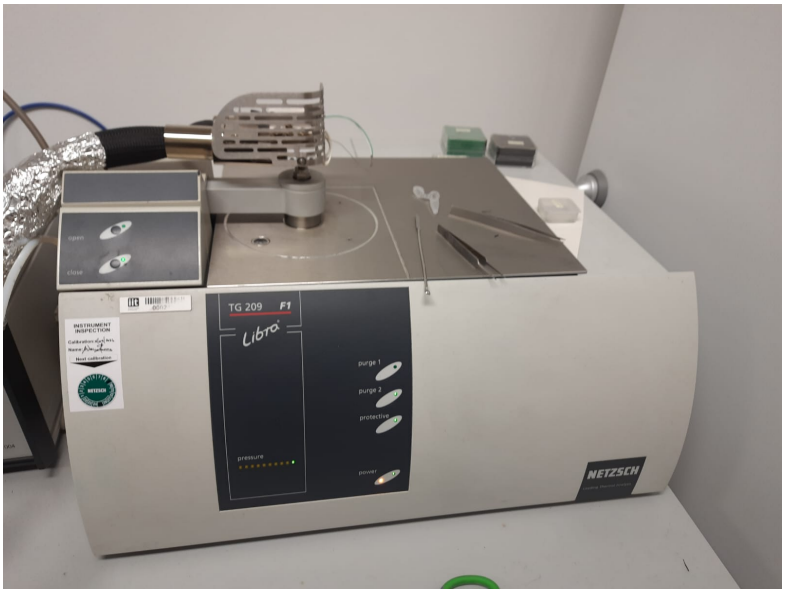

Figure 2.1: TGA instrumentation used.

2.1.2 DSC

The Differential Scanning Calorimetry (DSC) is a technique used to study phase transitions in a sample and the corresponding temperatures at which they occur. This method is particularly useful for identifying unknown samples, analyzing polymorphism, and determining the purity of materials.

The instrument setup consists of a scale with two crucibles made of inert materials: one holds the sample, while the other serves as a reference. A furnace controls the temperature during the analysis according to a specified thermal ramp. The atmosphere is typically inert to prevent reactions during the heating process. The DSC measures the amount of energy required to maintain both crucibles at the same temperature. Any phase transition in the sample, such as melting or crystallization, causes either exothermic or endothermic reactions, leading to temperature variations. Thermocouples within the furnace record these changes and transmit the data to a computer for analysis.

The result is a plot with heat flow on the y-axis and temperature on the x-axis. The baseline is generally a horizontal line, with peaks corresponding to phase transitions. The orientation of the peaks depends on the convention used. In the "exo up" convention, exothermic transitions appear as positive peaks while in the "endo up" convention, endothermic transitions appear as positive peaks. It is essential to specify the convention used on the plot for proper interpretation.

DSC is especially valuable for characterizing polymer materials because it identifies key thermal transition temperatures, including Glass Transition Temperature

(Tg), the temperature at which the polymer changes from a glassy state to a rubbery state, Crystallization Temperature (Tc), the temperature at which the polymer crystallizes, Melting Temperature (Tm), the temperature at which the polymer melts and Degradation Temperature (Td), the temperature at which thermal degradation begins.

The instrument used in this thesis work, as shown in Figure 2.2, is the NETZSCH DSC 204 F1 Phoenix.

Figure 2.2: DSC instrumentation used.

2.1.3 EIS

One of the most commonly used techniques to determine the capacitance or pseudo-capacitance of a supercapacitor device is Electrochemical Impedance Spectroscopy (EIS). This technique employs a potentiostat to apply either a sinusoidal potential or a sinusoidal current to the system. When a potential is applied, the method is known as Potentiostatic Electrochemical Impedance Spectroscopy (PEIS). In response, the system produces a sinusoidal current with the same frequency and characteristics as the applied potential.

The analysis involves applying a signal within a fixed potential range while varying the frequency. The resulting current is recorded for each frequency and plotted on a spectrum. The system's response is termed impedance and can be represented on a Nyquist plot, where the real (Z') and imaginary (Z") components of the impedance are displayed as (Z",Z') coordinates. Each point on the plot

corresponds to an experimental frequency. The intercept of Z' on the real axis represents the system's ohmic and/or Faradaic resistances. The imaginary component, Z", is related to the capacitance by Equation 2.1, which allows capacitance (C) to be determined as a function of frequency.

$$Z'' = \frac{1}{j\omega C} \tag{2.1}$$

EIS is particularly useful for distinguishing pseudocapacitive behavior from double layer capacitance across a range of frequencies, enabling more detailed characterization of the device.

The impedance behavior of simple systems can be recognized from the Nyquist plot. For an Ohmic resistance, R, the impedance is frequency independent, and the phase angle is zero, leading to Z'=R. A pure capacitive component has a phase angle of 90° and a frequency dependent imaginary impedance that follows Equation 2.1.

However, electrode/solution systems, especially those involving porous, high surface area materials, such as those used in supercapacitors, typically exhibit complex combinations of capacitive and ohmic behavior, often with pseudocapacitive contributions. As a result, the Nyquist plot becomes more intricate and must be carefully analyzed to fully understand the system [54].

Figure 2.3 illustrates common Nyquist plots for different types of devices.

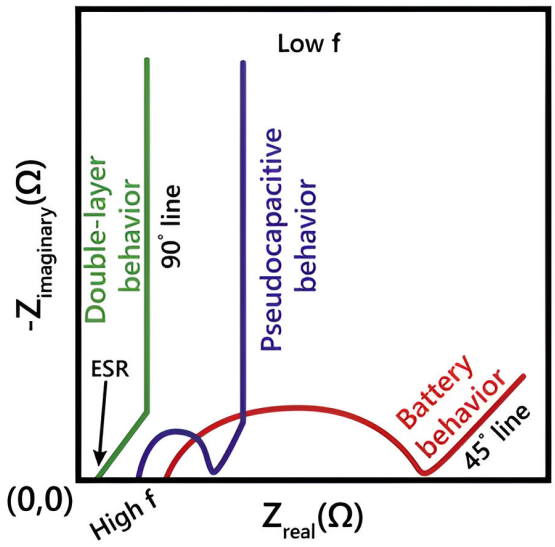

Figure 2.3: Typical Nyquist plots of various types of device [1].

2.1.4 CV

Cyclic Voltammetry (CV) is an electrochemical technique commonly used to characterize supercapacitors. In CV, a voltage sweep is applied repetitively, generating a current that depends on both time and potential. At the end of each potential cycle, the current direction is reversed, producing a distinctive current response.

For an ideal device with constant capacitance (C), the resulting CV plot has a rectangular shape, symmetrical around the zero current line. This symmetrical shape is often considered a criterion for evaluating the reversibility of the charge and discharge processes in supercapacitors. However, real electrochemical devices typically do not exhibit perfect symmetry, as capacitance often varies with voltage, especially when pseudocapacitive effects are present.

In contrast, battery type devices generally display asymmetric CV plots with no mirror symmetry. This is due to the occurrence of irreversible oxidation and reduction reactions during the charging and discharging cycles.

It is also important to note that some reversible, diffusion controlled reactions can lead to non mirrored plots. This behavior is usually due to different potentials being required for the anodic and cathodic reactions [1].

The typical CV plots for various device types are illustrated in Figure 2.4.

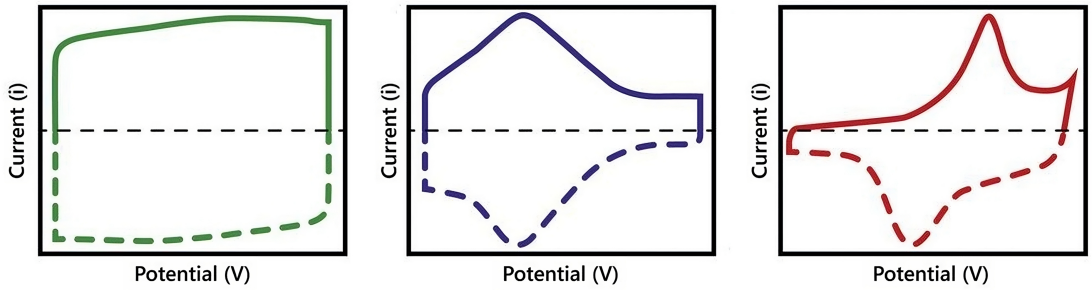

Figure 2.4: From left to right, common CV plots for: a supercapacitor, a pseudocapacitive device and a battery [1].

From a CV analysis, the Coulomb Efficiency of the tested device can be obtained. Coulomb Efficiency is defined by Equation 2.2, where Q_c and Q_d represent the charge during charging and discharging, respectively. These values are derived by integrating the current over time.

$$Coulomb\ Efficiency = \frac{Q_d}{Q_c} \cdot 100 \tag{2.2}$$

The Coulomb Efficiency indicates how much of the energy absorbed by the device during charging is recovered during discharge. Ideally, electric double layer (EDL) and pseudocapacitive phenomena, due to their reversible nature, should

return nearly all the absorbed energy. In contrast, faradaic reactions are typically irreversible, leading to energy dissipation.

The primary purpose of Coulomb Efficiency analysis is to determine the maximum potential range in which an electrode can operate with a given electrolyte. This potential window is typically explored through two sequential steps: the anodic and cathodic scans.

In the anodic scan, the device undergoes repeated CV with progressively increasing final potentials, starting from the open circuit potential. This continues until a noticeable reduction in Coulomb Efficiency is observed, marking the end of the anodic window and the onset of irreversible phenomena within the device.

The cathodic scan follows a similar approach but focuses on identifying the lowest potential before a decline in Coulomb Efficiency occurs.

The settings of this analysis are critical for accurately determining the potential window. A lower scan rate allows for a more precise measurement of efficiency loss but also increases device degradation, as it remains at voltages where irreversible processes occur for a longer duration. Additionally, lower scan rates extend the total analysis time.

From the maximum applicable potential, the total capacitance C_T is calculated using Equation 2.3, where the integral of the discharge current over time is divided by the maximum potential V_0.

$$C_T = \frac{\int i \, dt}{V_0} \tag{2.3}$$

2.1.5 FESEM

The Field Emission Scanning Electron Microscope (FESEM) is a high resolution electron microscope commonly used for surface analysis, capable of producing micrographs with nanometer scale resolution. This high resolution is achieved due to the short mean free path of the electrons, even when projected at high energies.

FESEM measurements must be conducted in an ultra high vacuum environment (10^{-8} Torr) to prevent gas ionization inside the chamber, which could interfere with the electron beam.

The electron source in FESEM typically consists of a sharp tungsten tip that acts as a cathode, positioned in front of a metal grid anode. When a high voltage is applied, an electron beam is generated and collimated using electromagnetic coils or charged plates to achieve the desired beam thickness. A thinner electron beam provides higher resolution but may also introduce more noise, whereas a thicker beam reduces noise but sacrifices resolution. Lenses within the microscope focus the beam onto the sample surface. Upon interaction with the sample, secondary electrons are emitted, which are then collected by a scintillator to generate an optical image.

To obtain high quality FESEM micrographs, proper sample preparation is essential. First, the sample must not release gases or degrade under vacuum conditions, as this could damage the instrument or interfere with the electron beam. Second, ince FESEM relies on electron interactions, non conductive samples must be coated with a thin layer of a conductive metal, like platinum or gold, via sputter coating to ensure accurate imaging and prevent charging effects.

The instrument used in this thesis work, as shown in Figure 2.5, is the Zeiss Supra 40.

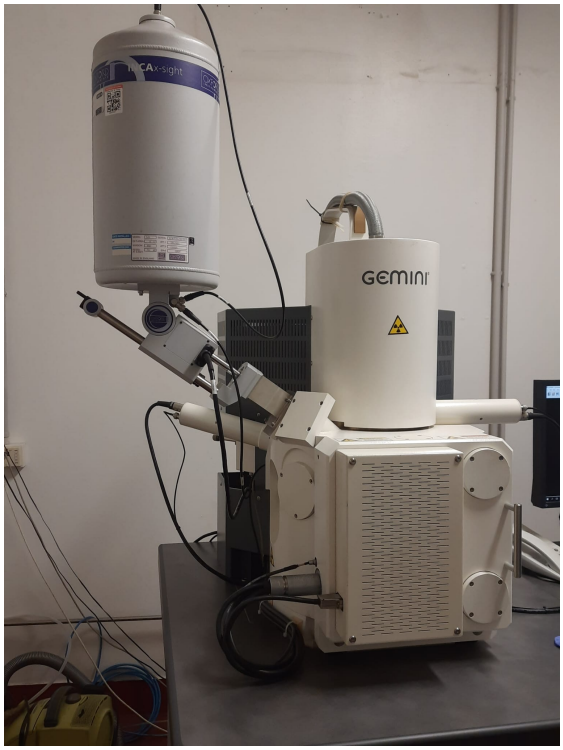

Figure 2.5: FESEM used.

2.2 Devices used for electrical characterizations

2.2.1 EL-Cell

The first cell architecture used in this thesis is the commercially available EL-Cell, which features a layered structure as shown in Figure 2.6. The EL-Cell is a reusable device, designed for easy assembly and disassembly, making it ideal for the study and characterization of polymer electrolytes. Its spring and screw support system

ensures constant and uniform pressure, optimizing contact between the electrodes and electrolytes, essential for accurate electrical measurements.

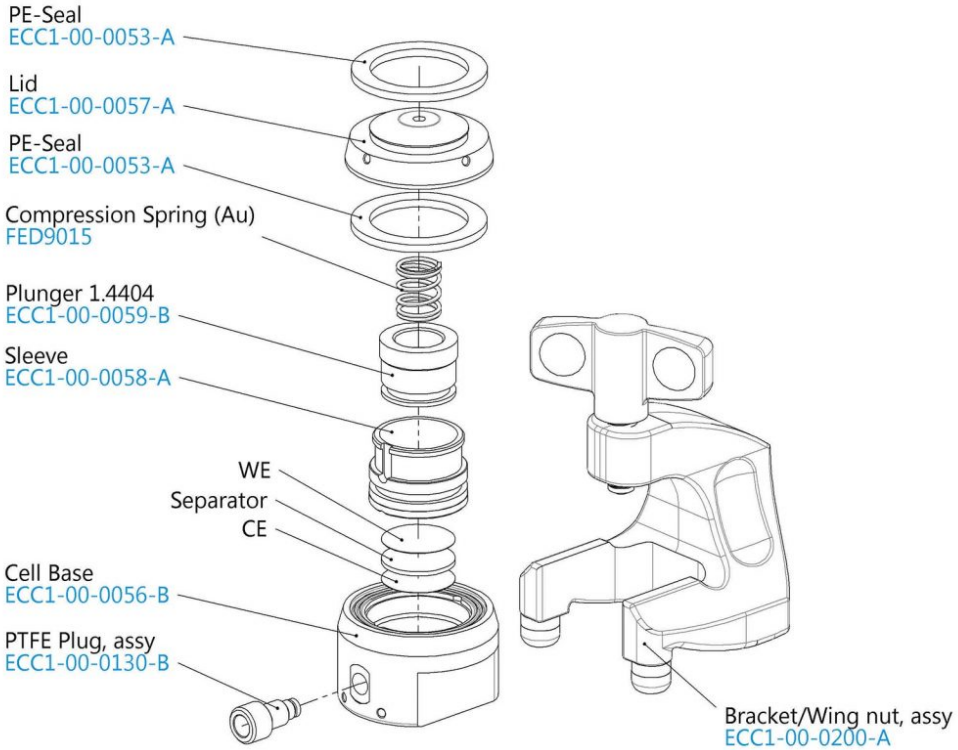

Figure 2.6: Structure of a EL-Cell [55].

In this work, the EL-Cell was used for preliminary tests to investigate the electrical behavior of the ionogels. However, it was eventually replaced by another setup due to its inability to precisely control the distance between electrodes, a limitation inherent to its manual screw based system.

2.2.2 Coin Cell

The second type of cell architecture used in this study is the coin cell, with its layered structure illustrated in Figure 2.7. These cells were employed to test the ELDCs, where the fabricated ionogels served as both the electrolyte and separator. The inclusion of a spacer and a spring was crucial to maintaining uniform pressure between the two electrodes, ensuring the proper functioning of the device.

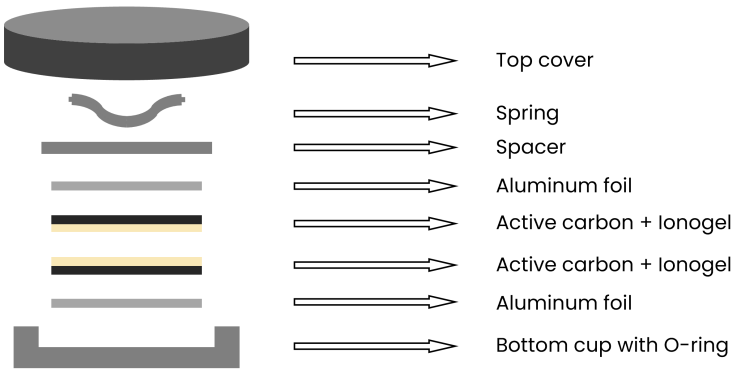

Figure 2.7: Structure of a coin cell.

2.3 Materials

PVDF-HFP pellets (Sigma-Aldrich, Poly(vinylidene fluoride-co- hexafluoropropylene), average Mw ~455,000, average Mn ~110,000) were used as the polymer matrix for the ionogels. Pyr_{14}TFSI (Solvionic, 1-Butyl-1-methylpyrrolidinium bis (trifluoromethanesulfonyl)imide, 99.9%, reference PYR0408A) was employed as the ionic liquid. Acetone (Sigma-Aldrich, suitable for HPLC, $\geq$ 99.9%) served as the solvent for the various solutions.

SiO_2 nanoparticles (MCM-41 NANO silica, synthesized in the lab following the method described in [56]) with diameters ranging from 20 to 50 nm, and GO flakes (Cheap Tubes Inc.; Size: <450nm X & Y; Thickness: 0.7-1.2 nm by AFM; Solubility: DI Water, NMP, DCB, or DMF; Purity: 99wt%; Elemental Analysis: C: 35-42%, O: 45-55%, H: 3-5%) of 300-800 nm in length and 0,7-1,2 nm in thickness were used to enhance the electrical properties of the electrolytes.

The activated carbon used for both electrodes of the coin cells was produced in the pilot line at the Environmental Park laboratories using a solution composed of YP50F [57], CMC (MTI Corporation, Carboxymethyl Cellulose (CMC) for Li-ion Battery Anode 100g/bottle - Lib-CMC) and CB (MTI Corporation, SUPER C65 Conductive Carbon Black as Conductive Additive for Lithium-Ion Batteries, 70g/bag - ELib-SC65) in ratio 85:5:10 respectively.

2.4 Characterization of the liquid solutions

To investigate the behavior of Pyr_{14}TFSI and its interactions with the nanoparticles, three solutions were prepared for various analyses. The composition of these

solutions is detailed in Table 2.1, and they are designated as IL, IL+SiO_2, and IL+GO for future reference. The solutions containing NPs were synthesized through simple direct mixing, followed by a 3 hour sonication process to ensure proper dispersion.

Name	Composition
IL	Pyr_{14}TFSI 100%
IL+SiO_2	Pyr_{14}TFSI 98,9% + SiO_2 1.1%
IL+GO	Pyr_{14}TFSI 99,8% + GO 0.2%

Table 2.1: Compositions of the prepared solutions.

The viscosity of these three solutions was analyzed using a rheometer equipped with parallel plates of 2.5 cm in diameter. The viscosity was calculated as a function of shear rate, with a plate gap of 0.2 mm and a shear rate range between 10^1-10^4 1/s. The instrument was equipped with a Peltier cell, enabling measurements across a temperature range from 5°C to 70°C.

The next step was to measure the conductance of these solutions to better understand the role of NPs in the ion transportation process. This analysis was also performed using the rheometer, which allowed precise control of both the electrolyte thickness and temperature. The two plates of the rheometer served as electrodes, connected to a potentiostat with an aluminu bridgle as illustrated in Figure 2.8.

PEIS analyses were conducted on the solutions at various temperatures. The applied frequency ranged from 10^6 to 10^2 Hz, with 10 data points collected per decade. The plate gap was set to 0.1 mm, and the temperature range spanned from 5°C to 70°C. Three measurements for each temperature were obtained to be sure of the thermal equilibrium state of the system.

2.5 Syntesis of the ionogels

The ionogels produced can be categorized into two families. The first consists of membranes containing only polymer, solvent, and ionic liquid, while the second includes membranes with nanoparticles introduced into the solution.

The first category of membranes was prepared using simple direct mixing. First, the desired weight of PVDF-HFP pellets was taken from a glovebox and placed in a vial. Acetone was then added, and the mixture was stirred for 1 hour at 40°C to dissolve the polymer. The appropriate quantity of Pyr_{14}TFSI was subsequently introduced into the vial using a syringe, and the vial opening was sealed with hot glue. The solution was stirred for an additional hour at 40°C.

Figure 2.8: Setup for PEIS analyses: on the left, the rheometer attached to the potentiostat to the right.

Finally, the membrane was cast onto aluminum foil using a Dr.Blade with a thickness setting of 0.5 mm. The ionogels were left to dry for a few minutes to allow for acetone to evaporate. The setup used is shown in Figure 2.9.

In this first family of membranes, five different ionogel solutions were prepared, maintaining a constant weight ratio of PVDF-HFP to acetone at 1:11.5. The ratios of PVDF-HFP to $Pyr_{14}TFSI$ varied from 1:2 to 1:5, as detailed in Table 2.2. The ionogel with a 1:4 polymer to ionic liquid ratio will be referred to as IG1 from this point forward.

Ratio polymer to IL	**PVDF-HFP**	**Acetone**	**$Pyr_{14}TFSI$**
1:2	6,89%	79,31%	13,80%
1:3	6,45%	74,19%	19,36%
1:4 (IG1)	6,06%	69,69%	24,25%
1:5	5,71%	65,71%	28,58%

Table 2.2: Composition of the ionogel solutions without NPs.

Figure 2.9: On the left, the setup for the production of the ionogel solutions; on the right, the Dr.Blade used for casting.

The second category of membranes was also prepared using a simple direct mixing method. The primary difference was the addition of the chosen weight of nanoparticles to the vial containing the polymer and acetone. The solutions were sonicated for 3 hours to ensure proper dispersion of the NPs and to prevent agglomeration. The mixture was then stirred for 30 minutes at 40°C. $Pyr_{14}TFSI$ was added as previously described, and the solution was stirred for another 30 minutes at 40°C before being cast using a Dr.Blade set to a thickness of 0.5 mm. The membranes were then left to dry.

Four membranes containing NPs were produced: two with 5 wt% SiO_2 and two with 1 wt% GO, based on the polymer weight. The PVDF-HFP to acetone ratio was maintained at 1:11.5, while the PVDF-HFP to $Pyr_{14}TFSI$ ratios used were 1:4 and 1:5. The compositions of the four solutions are listed in Table 2.3.

Name	Ionogels with NPs	PVDF-HFP	Acetone	$Pyr_{14}TFSI$	SiO_2	GO
IG2	1:4+SiO_2	6.04%	69.49%	24,17%	0,30%	-
IG3	I:5+SiO_2	5,69%	65,54%	28,49%	0,28%	-
IG4	1:4+GO	6.06%	69.25%	24.25%	-	0.08%
IG5	1:5+GO	5.71%	65.68%	28.56%	-	0.05%

Table 2.3: Composition of the ionogel solutions with NPs.

2.6 Characterization of the electrolytes

The conductance of the ionogels was determined using PEIS analyses with the same setup previously discussed and illustrated in Figure 2.8. A piece of the ionogel was placed between the two plates of the rheometer, and excess membrane was trimmed to form a disc, as shown in Figure 2.10.

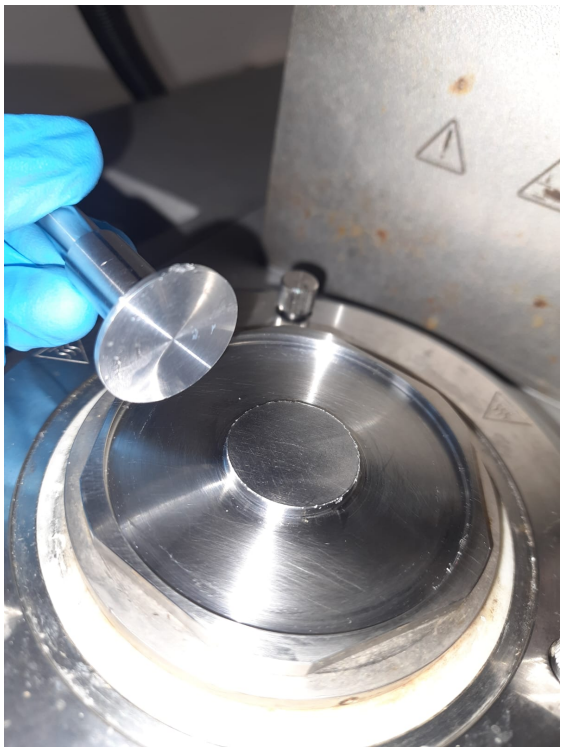

Figure 2.10: Ionogel disc after an experiment.

The applied frequency ranged from 10^6 to 10^2 Hz, with 10 data points collected per decade. The plate gap was set to 0.05 mm, and the temperature range remained the same as before, from 5°C to 70°C. Five ionogels were analyzed: the ionogel with a 1:4 polymer to ionic liquid ratio IG1, and the four ionogels containing

nanoparticles. As in previous analyses, three measurements were taken at each temperature to ensure the system had reached thermal equilibrium.

TGA analyses were conducted to study the degradation behavior of IG1, IG2, and IG4. The temperature range selected was from 30°C to 800°C, with a heating rate of 20 K/min.

DSC analyses were performed to investigate the thermal behavior of the ionogels as a function of temperature. Pure PVDF-HFP in pellet form and the ionogels IG1, IG2, and IG4 were selected for this study. These ionogels share the same polymer to IL ratio, allowing for a clearer understanding of the influence of nanoparticles on membrane behavior. The temperature range chosen for this analysis was from -70°C to 100°C, with a heating rate of 10 K/min.

FESEM analyses were carried out on IG2, IG3, IG4, and IG5 to examine the structure of the membranes and the dispersion of nanoparticles. The samples were prepared by tearing small pieces of the ionogels, which were then mounted on the holders and sputtered with platinum to enhance visibility under the microscope.

2.7 Fabrication of the devices

A strip of aluminum foil coated with activated carbon was removed from the oven where it had been stored. The strip was then secured to the working table using Kapton tape to prevent any unintended movement. The electrolyte solution was applied to the activated carbon using a DrBlade set at 350 micrometers. A section of the strip was intentionally left uncoated to allow for weighing the amount of activated carbon used in the spread.

Ten discs, each 15 mm in diameter, were cut using a puncher, with baking paper placed on top to protect the electrolyte layer. Figure 2.11 shows the obtained discs for both the carbon coated with IG3 and IG5, while Figure 2.12 presents the puncher itself. Additionally, six discs containing only activated carbon were obtained from both sheets and weighed to determine the amount of active material used in each device. The weight of the activated carbon electrode disc from the sheet with SiO_2 was 5,1 mg, while the one with GO weighed 5,7 mg. These values were derived from the average weight of the six activated carbon discs, subtracting the weight of the thin aluminum foil on which they were cast, measured at 4.35 mg/cm^2. It must be noted that the total active carbon weight per device should be doubled, as two identical electrodes were used.

The discs were then inserted into standard coin cells CR2032. The devices were sealed using a crimper set to a pressure of 9 bar. Figure 2.13 illustrates the crimper along with the various components of the coin cells. Five coin cells were assembled for both IG3 and IG5. Immediately after assembly, each device was tested using a bench multimeter shown in Figure 2.14 to check for short circuits. All ten coin

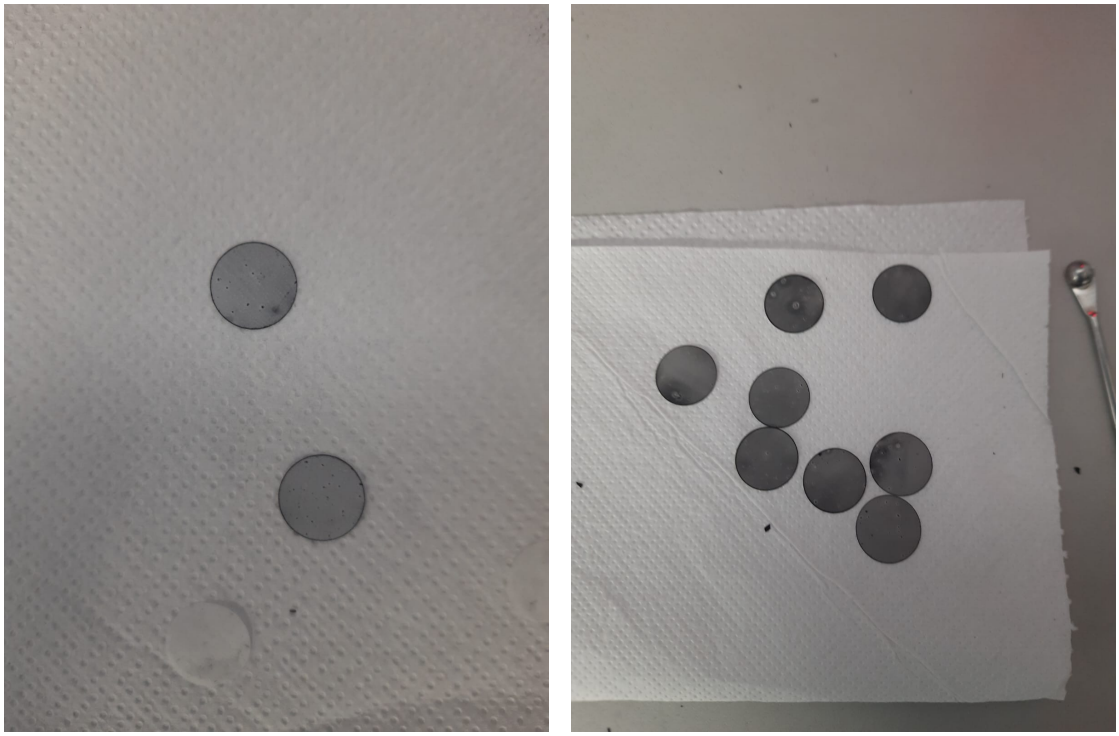

Figure 2.11: On the left, discs coated with IG3 while on the right, discs coated with IG5.

Figure 2.12: Puncher used.

cells were confirmed to be functional.

The device fabrication was conducted in a dry room environment to prevent

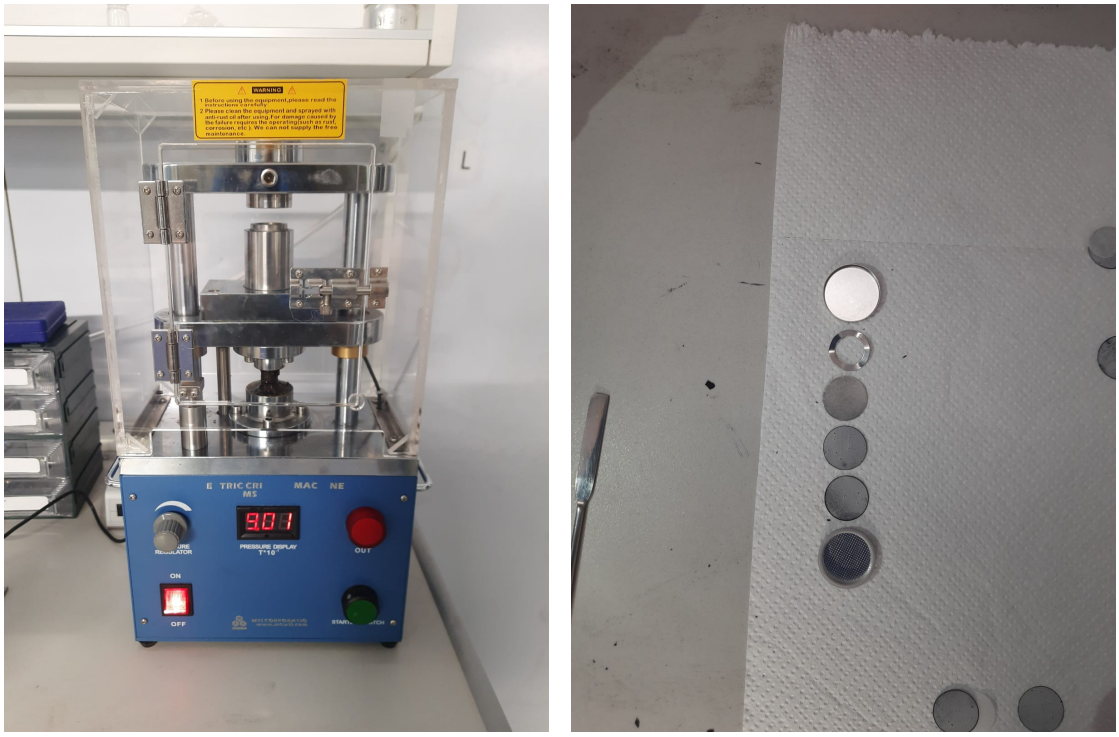

Figure 2.13: On the left, the crimper used, while on the right, the various components of the coin cell.

Figure 2.14: Bench multimeter used for testing.

contamination of both the electrodes and electrolytes.

2.8 Testing of the devices

OCV and PEIS measurements were performed on all ten coin cells to evaluate their initial impedance behavior. The analysis was conducted in two stages: first on six cells, followed by four, using the cell holder shown in Figure 2.15.

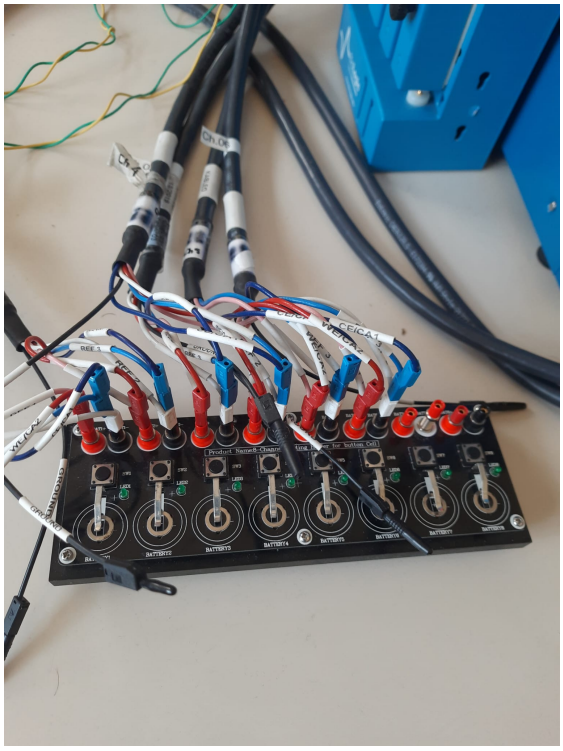

Figure 2.15: Cell holder used for testing.

The best performing coin cells for each series, the ones that resulted to be less resistive during the PEIS measurements, has then been analyzed in the range 5°C-70°C, to understand their behaviour in function of temperature.

Chapter 3

Results and discussion

3.1 Study of viscosity

As previously discussed, three liquid solutions containing the ionic liquid $Pyr_{14}TFSI$ and nanoparticles were analyzed using a rheometer to investigate their viscosity as a function of temperature. The primary objective of this analysis was to understand the potential role of NPs in modifying the viscosity of the solutions.

The temperature range selected for the study spanned from 5°C to 70°C, with increments of 5°C between 5°C and 20°C and increments of 10°C from 20°C to 70°C. Twelve droplets of each solution were deposited onto the bottom plate of the rheometer using a syringe, after which the top plate was positioned at a fixed distance of 0.2 mm via the instrument's software. Prior to the analysis, the samples were left at 5°C for 30 minutes to ensure thermal equilibrium.

A shear rate ranging from 10 1/s to 10^4 1/s was then applied to determine the viscosity. At each temperature change, the system was allowed to rest for 10 minutes to ensure thermal equilibrium. Figure 3.1 shows the viscosity results for IL (pure $Pyr_{14}TFSI$), IL+SiO_2 ($Pyr_{14}TFSI$ with SiO_2 NPs), and IL+GO ($Pyr_{14}TFSI$ with GO NPs), of which the compositions have already been reported in Table 2.1.

As observed in the plots, after a brief initial delay, the liquids behave like a Newtonian fluid showing a classic Newtonian plateau. This behavior remains consistent across the temperature range, although the overall viscosity of the system decreases with increasing temperature.

To better assess the role of NPs in the solutions, the viscosity at the Newtonian plateau was plotted as a function of temperature, as shown in Figure 3.2. The solutions containing NPs exhibit a behavior similar to that of pure $Pyr_{14}TFSI$, likely due to the low concentration of dispersed particles in the system.

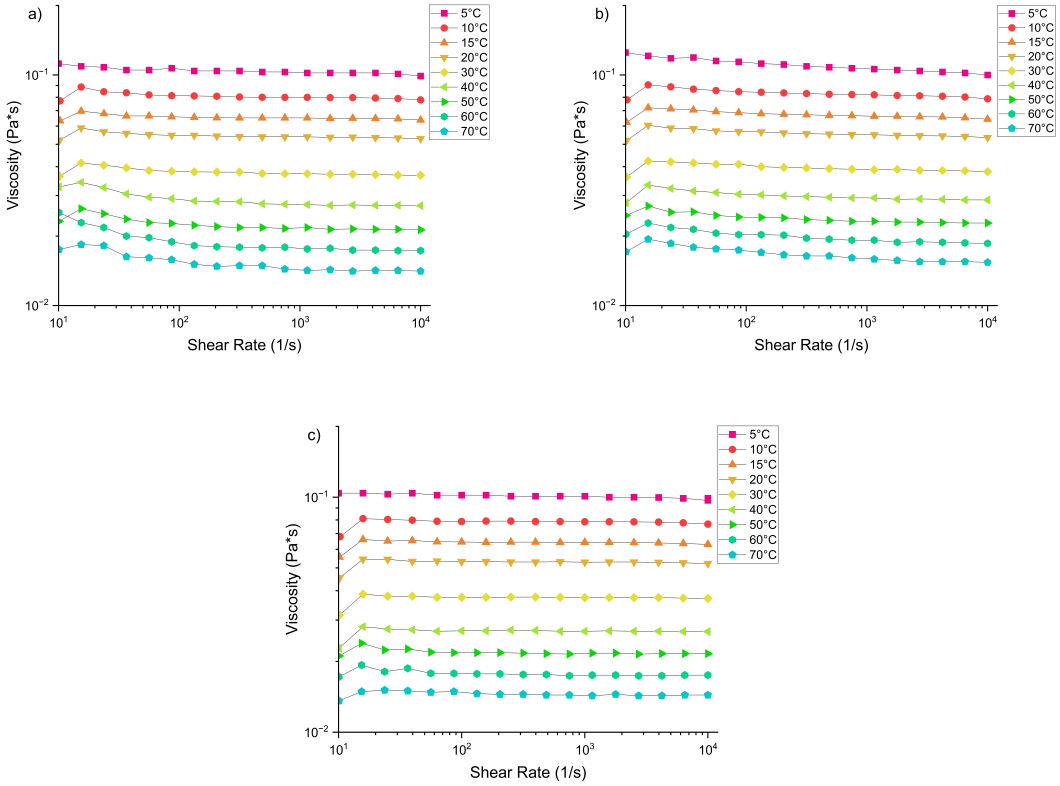

Figure 3.1: Viscosity results: a) IL, b) IL+SiO_2 and c) IL+GO.

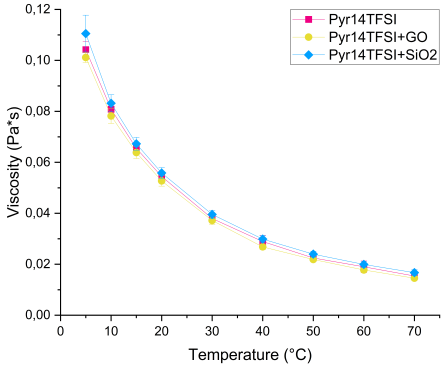

Figure 3.2: Viscosity comparison for the three solutions.

3.2 About the ionogels

As previously stated, ionogel electrolytes produced without the inclusion of nanoparticles, were made with a polymer to ionic liquid ratios ranging from 1:2 to 1:5 of which the compositions have already been reported in Table 2.2. The ionogels with ratios of 1:2, 1:3, and 1:4 proved to be self standing, as shown in Figure 3.3. Figure 3.3 also highlights the color differences among the three electrolytes. Increasing the IL content resulted in more transparent and wet membranes, with reduced mechanical strength. The ionogel with a 1:5 ratio was found to be too fragile to be peeled off from the aluminum foil on which it was cast. Therefore, the 1:4 ratio was identified as the highest possible to obtain a self standing electrolyte using only PVDF-HFP, $Pyr_{14}TFSI$, and acetone.

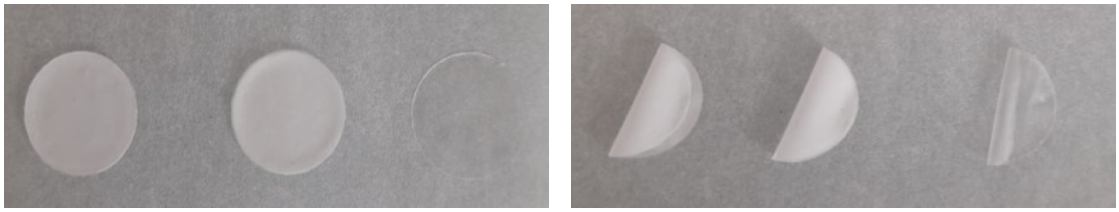

Figure 3.3: Color and self-standing properties of, from left to right, IG 1:2, IG 1:3 and IG 1:4.

The addition of NPs to the mixtures proved beneficial for the mechanical properties of the membranes, leading to sturdier ionogels. This improvement enabled a new test with the 1:5 ratio, successfully obtaining self standing membranes, as already shown in Table 2.3.

Regarding the electrical characterization of the ionogel electrolytes, the initial tests were conducted using an EL-Cell, primarily examining the membranes with 1:2, 1:3, and 1:4 ratios. A clear trend was observed, indicating that increasing the IL content enhances ionic conductivity. Based on this finding, further characterization was focused on the ionogels with a 1:4 ratio, assuming superior performance compared to the 1:2 and 1:3 ratio membranes.

3.3 TGA analyses

The TGA analyses were primarily conducted to evaluate the degradation process and thermal stability of the ionogel electrolytes and their components. As mentioned previously, the temperature range selected was from 25°C to 800°C, with a temperature ramp of 20 K/min. The analysis was carried out in an inert nitrogen atmosphere (N_2) to prevent oxidation of the species.

The ionogels analyzed were IG1, IG2, and IG4 to better understand the role of the NPs introduced into the solutions while maintaining a constant polymer to IL ratio of 1:4. The TGA analysis plots for these samples are shown in Figure 3.4.

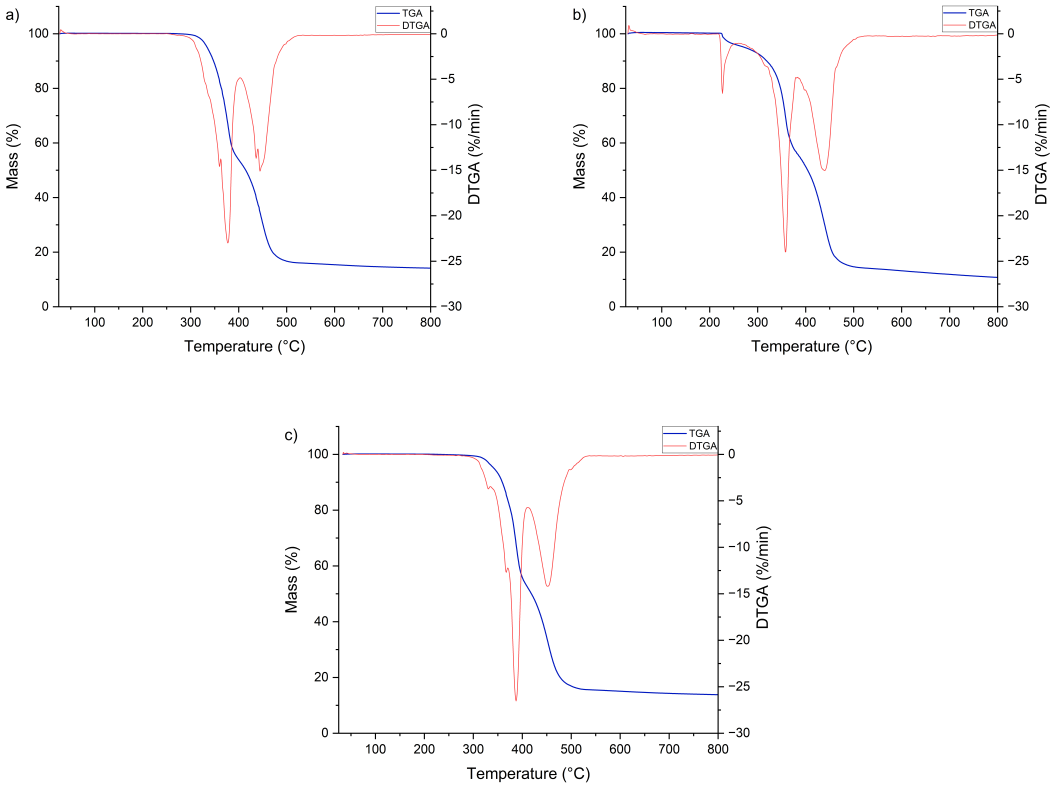

Figure 3.4: Results of the TGA analysis for: a) IG1, b) IG2 and c) IG4.

For the three electrolytes, the degradative process is mainly described by two steps, which are highlighted by the two peaks shown in the DTGA, the first derivative of the TGA curve. For IG1, the maximum degradation rates occur at 377°C and 445°C, with corresponding weight losses of 43.75% and 40.96%, respectively. After 500°C, 14.52% of the total weight remains. IG4 follows a similar degradation process, with the maximum degradation rates occurring at 386°C and 451°C. The weight losses are 44.65% and 40.96%, respectively, and after 500°C, the residual weight is 14.15%. In contrast, IG2 displays, in addition to the two main peaks at 356°C and 440°C, a third peak at 225°C, associated with a weight loss of 5.18%. The other two major weight losses are 40.62% and 40.41%, with a residual weight of 13.81% after 500°C.

To better understand the degradative process of the ionogels, TGA analyses of pure PVDF-HFP, $Pyr_{14}TFSI$, silica nanoparticles, and GO nanoparticles were conducted and are reported in Figure 3.5.

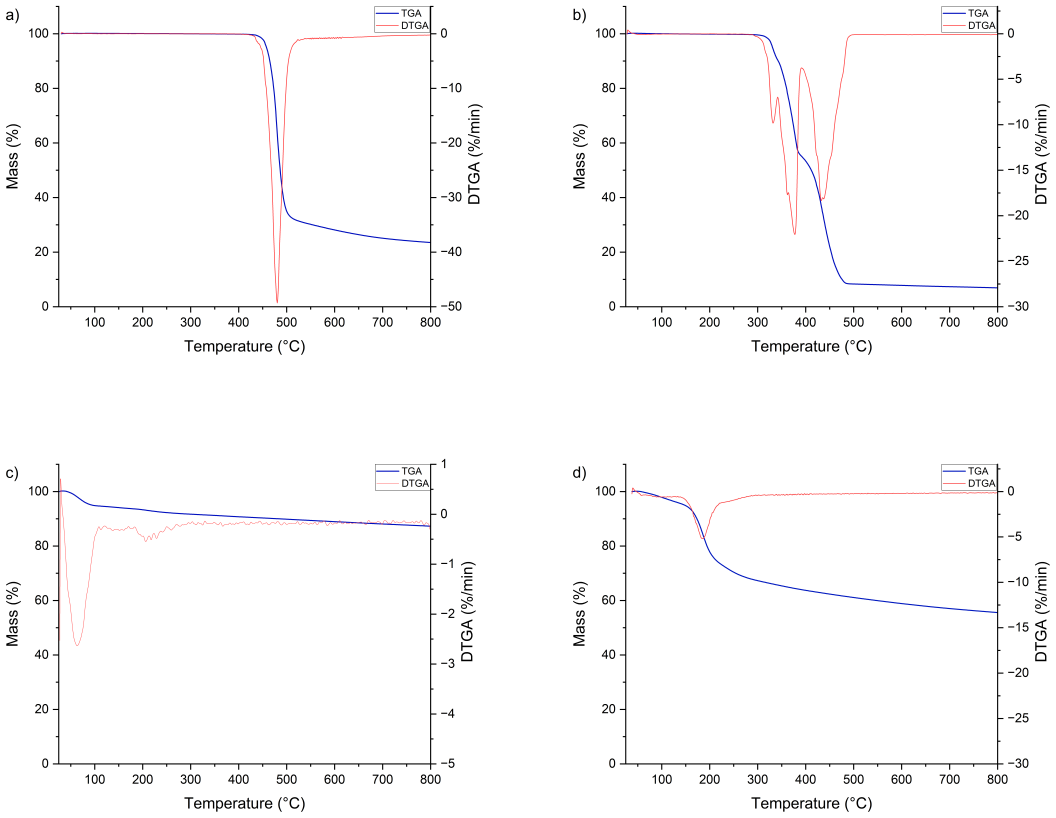

Figure 3.5: Results of the TGA analysis for: a) Pure PVDF-HFP, b) $Pyr_{14}TFSI$, c) SiO_2 NPs and d) GO NPs.

Pure PVDF-HFP pellets show a single degradation peak at 480°C with a weight loss of 69.41%, leaving a residue of 30.59% after 500°C. $Pyr_{14}TFSI$ exhibits two main degradation peaks at 377°C and 434°C, corresponding to weight losses of 43.28% and 48.67%, respectively, with 8.05% of the total weight remaining after 500°C. The third and smallest peak at lower temperature is considered a shoulder of the one at 377°C. The silica nanoparticles display two main degradation peaks: one at 63°C with a weight loss of 5.15%, and a broader peak in the 200-250°C range, with a weight loss of 3.42%. GO nanoparticles show a single degradation peak at 186°C, with a weight loss of 33.08%.

Comparing the results for the ionogels with those of the individual components,

it can be observed that the first degradation peak, occurring between 350-400°C, is attributed to the initial degradation step of $Pyr_{14}TFSI$. The second peak, around 450°C, is caused by a combination of the second degradation step of $Pyr_{14}TFSI$ and the degradation of PVDF-HFP. The residual products remaining after 500°C are likely a mixture of degradation products from both the ionic liquid and the polymer.

The degradation process of $Pyr_{14}TFSI$ requires further investigation. As previously mentioned, the degradation occurs in two main steps, which differs from the behavior reported in the literature, where a single degradation peak is typically observed in the 400–500°C range [58]. While the degradation pattern may depend on the synthesis method used for the ionic liquid, the exact nature of these two degradation steps remains unclear.

The most plausible hypothesis is that one peak corresponds to the degradation of the TFSI anion, while the other corresponds to the cation. To better understand these processes, FT-IR analysis of the degradation gases from the TGA experiment was conducted. The first peak showed spectral matches with HF, SO_2, and methylamine, suggesting that it corresponds to the decomposition of the TFSI anion. However, the spectra also showed similarities to butane, a compound that could only originate from the cation. The FT-IR spectrum of the first degradation peak is shown in Figure 3.6, with the identified possible compounds highlighted in different colors.

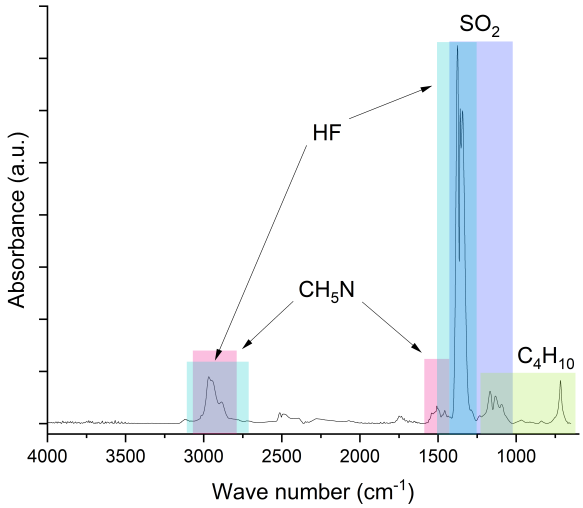

Figure 3.6: FT-IR spectrum of the gases freed in the first degradation step of $Pyr_{14}TFSI$.

Moreover, the FT-IR spectrum of the second peak were particularly difficult to analyze and compare with known reference spectra, making it challenging to draw definitive conclusions. As a result, the degradation behavior of $Pyr_{14}TFSI$ remains inconclusive and warrants further study in future analyses.

The degradation peaks observed for SiO_2 nanoparticles are attributed to the desorption of physically absorbed water and the release of condensation water from the interaction of the SiOH groups on the surface of the particles, occurring in the temperature ranges of 50-150°C and 200-300°C, respectively. A similar behavior is observed in IG2, with the degradation peak at 225°C corresponding to the second of these two phenomena.

The main degradation peak for GO nanoparticles is likely due to release of water from the surface of the NPs. IG4 does not exhibit this peak, likely due to the low concentration of GO nanoparticles in the solution and the production process of the electrolytes.

Overall, the ionogels exhibit excellent thermal stability, maintaining integrity up to temperatures exceeding 350°C before signs of degradation appear. This level of thermal stability is highly suitable for implementing IGs in EDLCs, enabling the devices to operate efficiently at high working temperatures.

3.4 DSC analyses

The DSC analyses were carried out to understand the behaviour of the ionogels in their working temperature range. The focus was the identification of possible phase transitions that could invalidate the electrical performance of the electrolytes. As stated before, the temperature range for the DSC analyses chosen was from -70°C to 100°C with a temperature ramp of 10 K/min. IG1, IG2 and IG4 were analysed to understand the role of NPs, while a pellet of pure PVDF-HFP was used as starting point for the study. In the setup, a first cooling was carried out from 25°C to -70°C to preserve the ionic liquid contained in the ionogels, followed by a first heating from -70°C to 100°. The procedure was then repeated for another cycle of cooling and heating, following the temperature range set for the analysis. It is important to remember that the first cooling and heating cycle is made to erase the thermal history of the samples, leaving the second cycle as the one useful for data analysis. The plots obtained from the DSC can be seen in Figure 3.7.

In all the four samples, after the first cycle, no visible phase transition can be seen, shown also by the study of the first derivative of the curves in Figure 3.8. The only disturbances in the plots are due to the switch of the engines used in the instrumentation to reach -70°C.

During the first heating cycle of pure PVDF-HFP, and to a lesser extent in the ionogels, a small peak appears in the 60°C-70°C range. This phenomenon, which

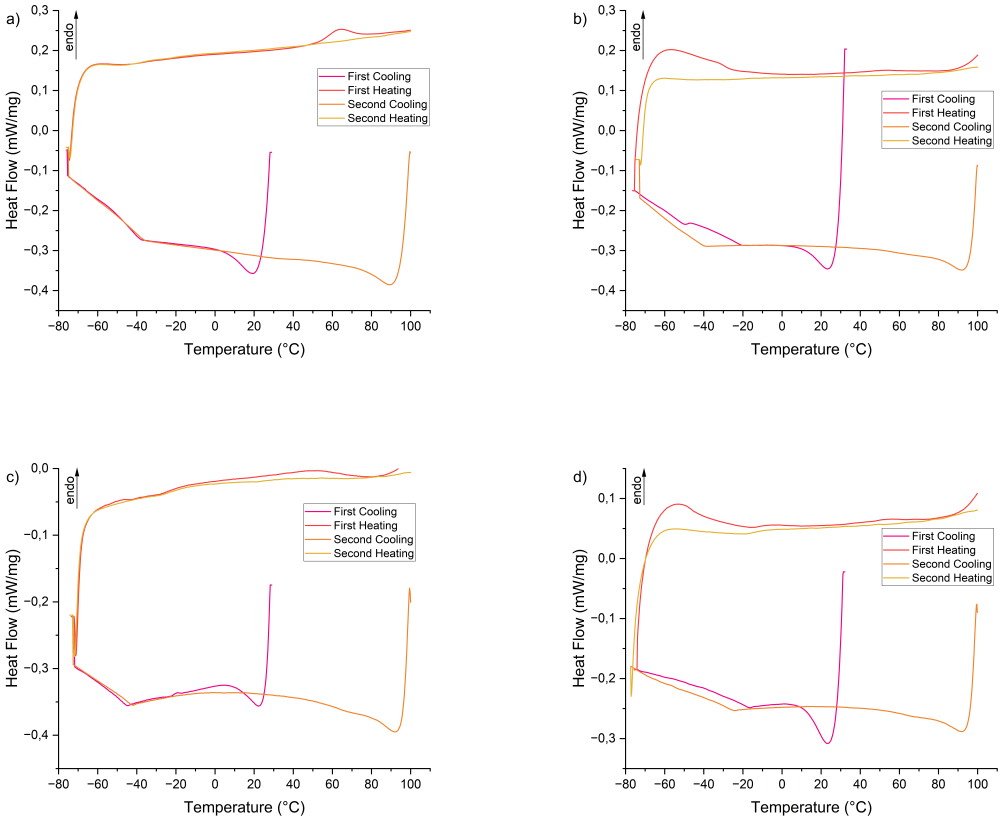

Figure 3.7: Results of the DSC analysis for: a) Pure PVDF-HFP, b) IG1, c) IG2 and d) IG4.

disappears in subsequent heating cycles, has been referred to in the literature as the "annealing peak" [59]. In semi crystalline polymers like PVDF-HFP, this peak may arise due to various factors, including the upper glass transition temperature, reorganization within conformationally disordered α crystals, molecular motions at the crystalline/amorphous interface, melting of paracrystalline domains, or a phase transition from the α phase to the β phase. However, DSC analysis alone cannot conclusively determine the nature of this peak, and further investigation would be required to fully understand its origin.

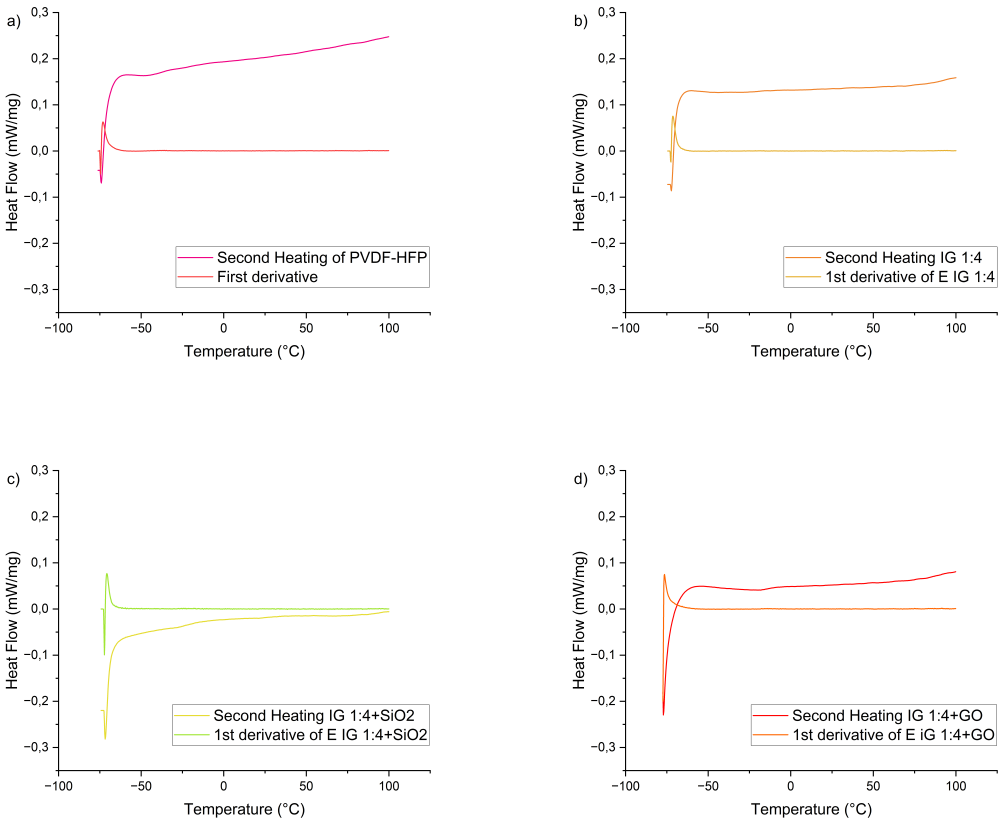

Figure 3.8: Study of the first derivative for the second heating cycle of the DSC analyses for: a) Pure PVDF-HFP, b) IG1, c) IG2 and d) IG4.

3.5 Conductance and electrical properties

EIS analyses were conducted at various temperatures to investigate the resistance behavior of the samples during heating. From the Nyquist plots, the equivalent series resistance was determined via linear interpolation of the capacitive region of the curve. Subsequently, the electrolyte capacitance was calculated using Equation 3.1, where R denotes the equivalent series resistance, A represents the plate area of the rheometer (fixed at 4.909 cm^2 for all calculations), and d corresponds to the distance between the plates, defining the electrolyte thickness. The results were then visualized in a plot, with conductance on the y-axis and 1/T on the x-axis, both in logarithmic scale, to emphasize the temperature dependence.

$$C = \frac{d}{R \cdot A} \tag{3.1}$$

As previously mentioned, three liquid solutions were tested to evaluate whether the introduction of nanoparticles could influence the electrical properties of the ionic liquid. Three possible behaviors were hypothesized: (i) the addition of NPs could enhance the ionic conductivity of the ionic liquid by facilitating ion transport and creating new pathways for ion movement; (ii) the presence of NPs could reduce ionic conductivity being external objects in ion pathways; or (iii) the NPs might have no significant effect on the conductivity of the ionic liquid.

The Nyquist plots of IL, IL+SiO_2, and IL+GO are shown in Figure 3.9, where a capacitive behavior is observed for all three solutions, accompanied by a decrease in resistance with increasing temperature. The solutions exhibit relatively low resistance, ranging from 0.5 to 2 Ω, depending on the temperature. The conductance of the solutions is plotted in Figure 3.10 as a function of 1/T and is also tabulated in Table 3.1.

Notably, the conductance of pure Pyr_{14}TFSI, measured at 2.563 mS/cm, is lower than the literature reported value of 3.2 mS/cm at 40°C. This discrepancy is likely due to the experimental setup used in this study, which looks to show higher resistance compared to other systems, such as the EL-Cell. Consequently, all conductance values obtained in this work might be higher if measured with alternative setups.

Regarding the influence of NPs, some discrepancies are observed among the three curves, with IL+SiO_2 exhibiting slightly higher conductivity and IL+GO slightly lower conductivity. These variations are likely attributable to instrumental factors. Therefore, it was concluded that the introduction of NPs in the solutions does not significantly affect conductivity, likely due to the low concentration of inclusions in the liquid phase.

PEIS analyses were also conducted for IG1, IG2, IG3, IG4, and IG5. As previously discussed, the primary expected outcome to obtain from these tests was an increase in the ionic conductivity of the ionogel electrolyte upon the introduction of NPs, as suggested in [52] and [53].

The Nyquist plots of the five electrolytes are presented in Figure 3.11. The most notable difference between the ionogels is the presence of a more pronounced initial semicircular feature in the electrolytes containing SiO_2 nanoparticles, IG2 and IG3, particularly at lower temperatures, which results in overall higher resistance compared to the other membranes. A similar trend of resistance reduction with increasing temperature is observed, consistent with the behavior found for the liquid solutions. Notably, IG2 and IG3 are the only membranes exhibiting an increase in resistance between 60°C and 70°C. This behavior will be further analyzed in the following section.

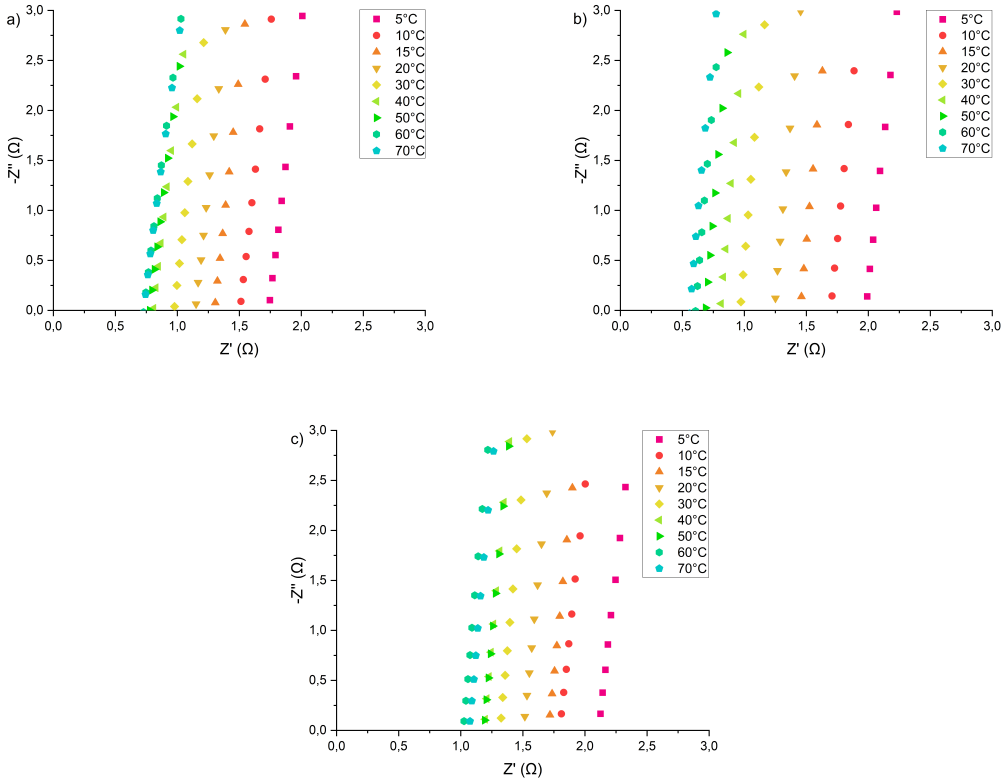

Figure 3.9: Nyquist plots for: a) IL, b) IL+SiO_2 and c) IL+GO.

The conductance of the electrolytes was calculated as previously described using Equation 3.1, and the results are shown in Figure 3.12, where the curve of pure $Pyr_{14}TFSI$ is also reported for comparison. Table 3.2 presents the conductance values for ionogels with a 1:4 polymer to ionic liquid ratio, while Table 3.3 reports the values for the electrolytes with a 1:5 ratio.

IG1, composed solely of PVDF-HFP and $Pyr_{14}TFSI$, serves as the reference to assess the impact of the inclusion of nanoparticles. At low temperatures, IG2 and IG4 exhibit conductance values in the range of 10^{-4} S/cm, lower than those of IG1. However, above 40°C, their performance improves, with IG4 reaching the highest conductance among all ionogel electrolytes at 70°C of 1.816 mS/cm. These results suggest that, while NPs may initially hinder ion transport in a less mobile system, at higher temperatures, increased system energy allows ions to use the new pathways made possible by the NPs surfaces, facilitating transport. The sharper slope of the IG2 and IG4 conductance curves compared to IG1 further supports this interpretation.

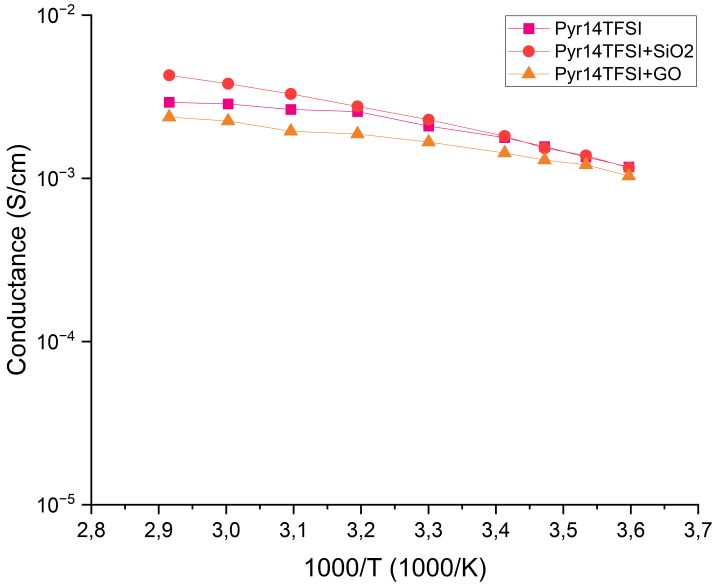

Figure 3.10: Comparison of the conductance of IL, IL+SiO_2 and IL+GO.

	IL		**IL+SiO_2**		**IL+GO**	
T (°C)	**C (mS/cm)**	**σ (mS/cm)**	**C (mS/cm)**	**σ (mS/cm)**	**C (mS/cm)**	**σ (mS/cm)**
5	1,172	$8{,}161 \cdot 10^{-3}$	1,164	$2{,}262 \cdot 10^{-2}$	1,032	$3{,}070 \cdot 10^{-3}$
10	1,354	$1{,}367 \cdot 10^{-3}$	1,384	$1{,}811 \cdot 10^{-2}$	1,216	$6{,}854 \cdot 10^{-3}$
15	1,568	$4{,}321 \cdot 10^{-3}$	1,532	$1{,}166 \cdot 10^{-2}$	1,295	$1{,}599 \cdot 10^{-2}$
20	1,784	$2{,}366 \cdot 10^{-3}$	1,828	$3{,}816 \cdot 10^{-2}$	1,431	$4{,}365 \cdot 10^{-3}$
30	2,095	$4{,}471 \cdot 10^{-3}$	2,297	$1{,}121 \cdot 10^{-1}$	1,677	$5{,}158 \cdot 10^{-3}$
40	2,563	$2{,}390 \cdot 10^{-2}$	2,765	$6{,}694 \cdot 10^{-2}$	1,871	$5{,}153 \cdot 10^{-3}$
50	2,641	$1{,}981 \cdot 10^{-3}$	3,296	$1{,}102 \cdot 10^{-2}$	1,949	$4{,}588 \cdot 10^{-2}$
60	2,857	$4{,}815 \cdot 10^{-2}$	3,823	$2{,}043 \cdot 10^{-2}$	2,373	$4{,}221 \cdot 10^{-3}$
70	2,923	$9{,}148 \cdot 10^{-2}$	4,284	$7{,}042 \cdot 10^{-2}$	2,257	$8{,}941 \cdot 10^{-3}$

Table 3.1: Conductance results for IL, IL+SiO_2 and IL+GO.

In contrast, IG3 and IG5 exhibit higher conductance across the entire temperature range compared to IG1, in agreement with the established trend that increasing the ionic liquid content enhances conductivity. IG3 performs particularly well between 5°C and 20°C, achieving the highest conductance at 5°C of 0.301

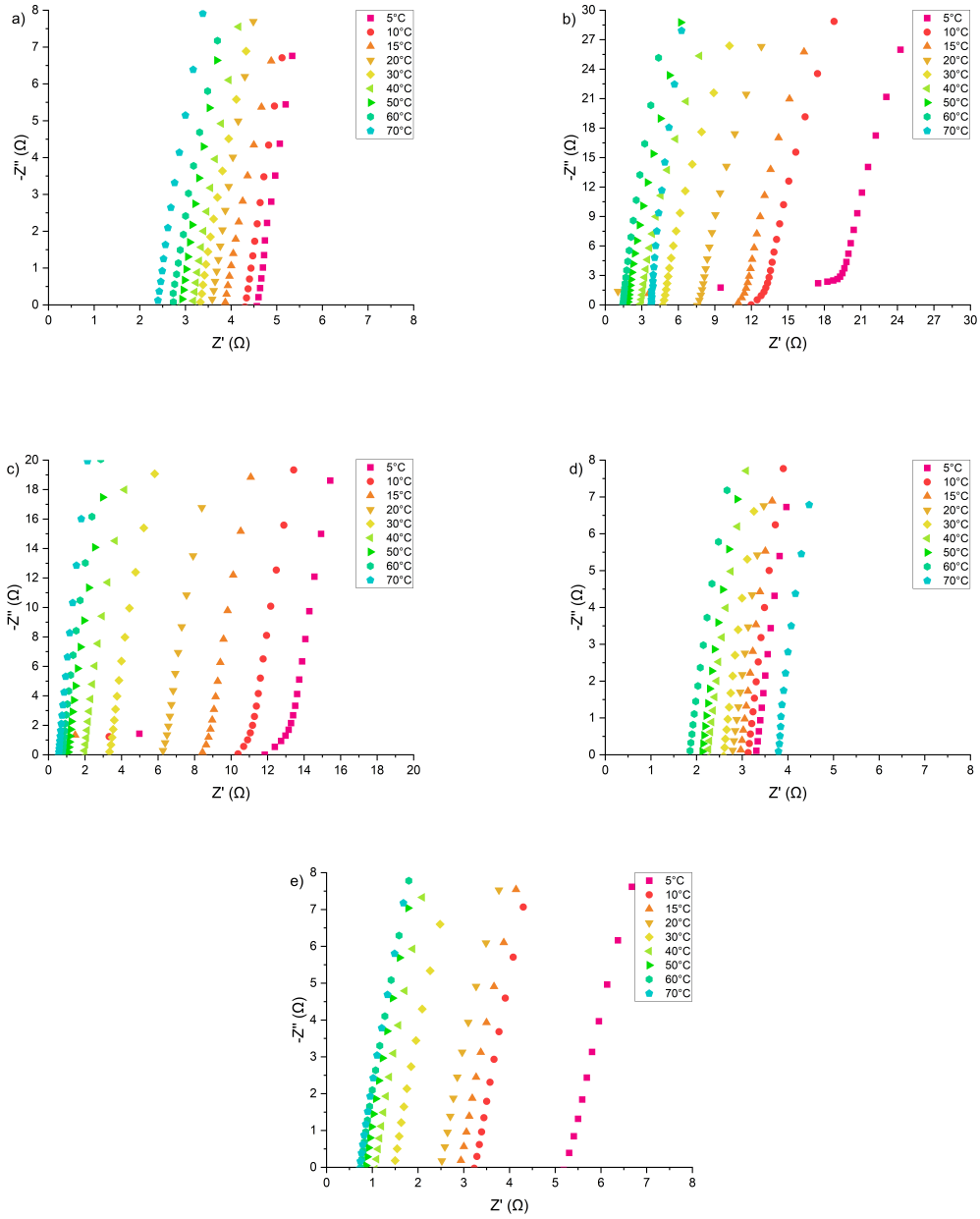

Figure 3.11: Nyquist plots for: a) IG1, b) IG2, c) IG4, d) IG3 and e) IG5.

mS/cm, while IG5 outperforms the others above 20°C.

It is also important to address the unusual behavior of IG2 and IG3 in the

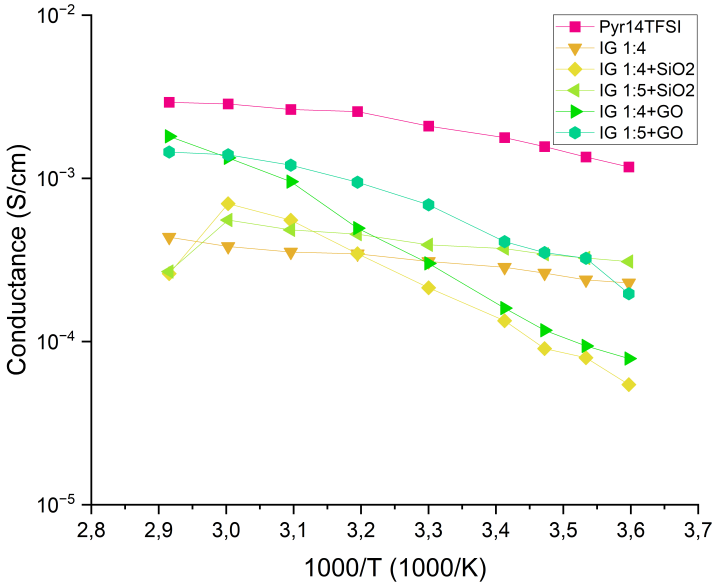

Figure 3.12: Comparison of the conductance of the various ionogel electrolytes compared to pure $Pyr_{14}TFSI$.

60°C–70°C range, where they are the only membranes showing a decrease in conductance. A possible explanation is the role of silica nanoparticles in the crystallization process of PVDF-HFP, which may lead to a reduction in the amorphous phase content and, consequently, lower conductance, while also taking into consideration the possible role of the "annealing peak" already discussed.

The introduction of GO flakes in the solutions appears to be more beneficial than the addition of SiO_2 nanoparticles, particularly at higher temperatures.

Ultimately, IG3 was identified as the best performing ionogel electrolyte at lower temperatures, while IG5 demonstrated superior performance for high temperature applications. Therefore, these two ionogels were selected for testing in an EDLC device.

3.6 FESEM micrographies

FESEM micrographs at various magnifications were taken for IG1, IG2, IG3, IG4, and IG5 to study the morphology of the electrolytes and the dispersion of nanoparticles.

The micrographs of IG1 reveal a homogeneous gel like structure consisting

	IG1		IG2		IG4	
T (°C)	**C (mS/cm)**	**σ (mS/cm)**	**C (mS/cm)**	**σ (mS/cm)**	**C (mS/cm)**	**σ (mS/cm)**
5	0,228	$3{,}784{\cdot}10^{-3}$	$5{,}440{\cdot}10^{-2}$	$2{,}438{\cdot}10^{-4}$	$7{,}860{\cdot}10^{-2}$	$1{,}095{\cdot}10^{-3}$
10	0,238	$7{,}106{\cdot}10^{-3}$	$7{,}959{\cdot}10^{-2}$	$3{,}104{\cdot}10^{-4}$	$9{,}390{\cdot}10^{-2}$	$1{,}120{\cdot}10^{-3}$
15	0,262	$2{,}324{\cdot}10^{-3}$	$9{,}052{\cdot}10^{-2}$	$1{,}790{\cdot}10^{-4}$	0,117	$1{,}419{\cdot}10^{-4}$
20	0,284	$2{,}123{\cdot}10^{-4}$	0,134	$1{,}073{\cdot}10^{-3}$	0,160	$1{,}306{\cdot}10^{-4}$
30	0,309	$4{,}435{\cdot}10^{-3}$	0,213	$6{,}830{\cdot}10^{-4}$	0,300	$8{,}980{\cdot}10^{-4}$
40	0,344	$1{,}957{\cdot}10^{-2}$	0,345	$8{,}104{\cdot}10^{-3}$	0,495	$1{,}233{\cdot}10^{-2}$
50	0,353	$4{,}393{\cdot}10^{-3}$	0,553	$2{,}272{\cdot}10^{-3}$	0,954	$4{,}124{\cdot}10^{-3}$
60	0,381	$3{,}909{\cdot}10^{-3}$	0,698	$4{,}798{\cdot}10^{-3}$	1,342	$9{,}651{\cdot}10^{-3}$
70	0,435	$6{,}690{\cdot}10^{-3}$	0,260	$8{,}462{\cdot}10^{-3}$	1,816	$9{,}777{\cdot}10^{-3}$

Table 3.2: Conductance results for IG1, IG2 and IG4.

	IG3		IG5	
T (°C)	**C (mS/cm)**	**σ (mS/cm)**	**C (mS/cm)**	**σ (mS/cm)**
5	0,308	$6{,}289{\cdot}10^{-3}$	0,196	$1{,}022{\cdot}10^{-2}$
10	0,324	$1{,}211{\cdot}10^{-3}$	0,323	$5{,}952{\cdot}10^{-4}$
15	0,342	$8{,}303{\cdot}10^{-4}$	0,350	$3{,}876{\cdot}10^{-4}$
20	0,371	$4{,}140{\cdot}10^{-4}$	0,409	$8{,}452{\cdot}10^{-4}$
30	0,391	$9{,}586{\cdot}10^{-4}$	0,688	$7{,}036{\cdot}10^{-3}$
40	0,454	$1{,}065{\cdot}10^{-3}$	0,947	$2{,}115{\cdot}10^{-2}$
50	0,483	$1{,}529{\cdot}10^{-3}$	1,226	$3{,}576{\cdot}10^{-3}$
60	0,555	$1{,}507{\cdot}10^{-3}$	1,401	$6{,}639{\cdot}10^{-3}$
70	0,268	$3{,}722{\cdot}10^{-3}$	1,454	$1{,}496{\cdot}10^{-2}$

Table 3.3: Conductance results for IG3 and IG5.

of polymer chains and ionic liquid, as shown in Figure 3.13. The spheroidal conformations appear to be on the micrometer scale.

IG2 and IG3 exhibit a similar structure to IG1, as seen in Figure 3.14 and Figure 3.15. A more detailed analysis was performed to locate the silica nanoparticles dispersed within the electrolyte. The silica particles identified in Figure 3.16 appear at the expected size. The low concentration of NPs in the solution results in a non homogeneous distribution, with regions rich in NPs and others completely bare. Some agglomerates were also observed, suggesting that further sonication may be

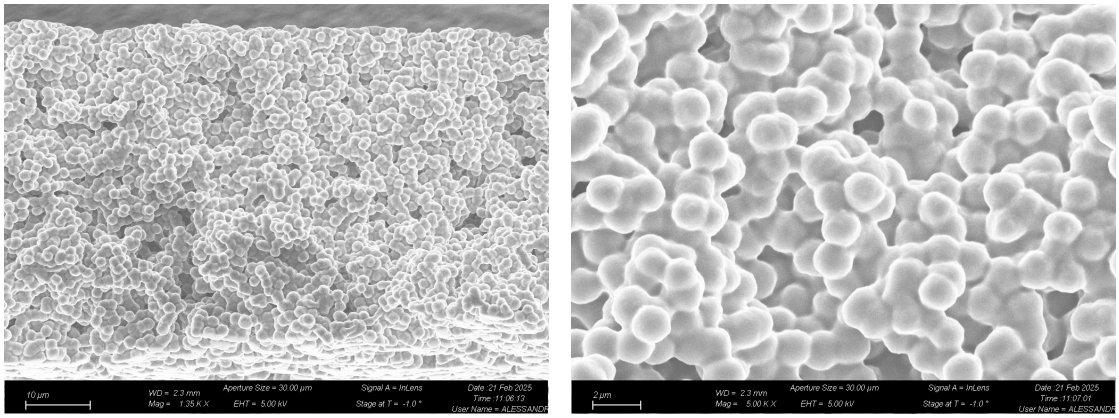

Figure 3.13: FESEM micrographs for IG1.

needed to improve dispersion.

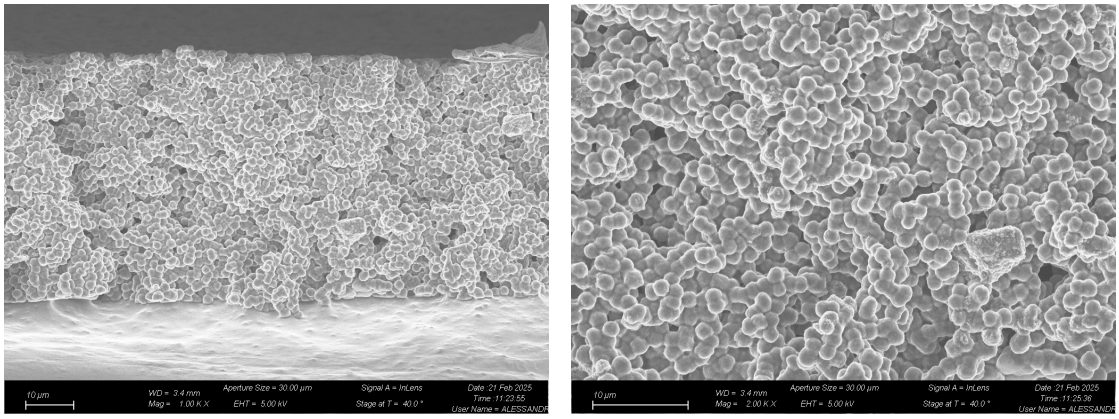

Figure 3.14: FESEM micrographs for IG2.

IG4 and IG5 follow the same structural trend as the other membranes, with a gel like structure, as shown in Figure 3.17. The GO flakes are clearly visible, adopting various conformations while situated between the spheroidal structures, as shown in Figure 3.18. Similar to the silica nanoparticles, the GO flakes are too few in number to achieve a uniform dispersion throughout the electrolyte. However, no agglomeration was observed in this case.

Although the dispersion of nanoparticles is not perfect, the quantity present appears sufficient to enhance the electrical properties of the electrolytes, as discussed in previous sections. This improvement likely arises from the nanoparticles' role in creating new pathways for ion transport, even if they are not directly involved in

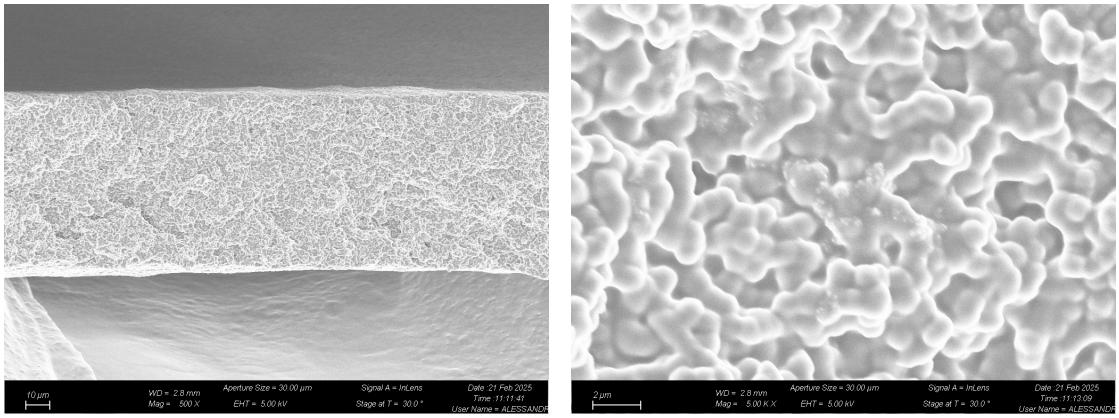

Figure 3.15: FESEM micrographs for IG3.

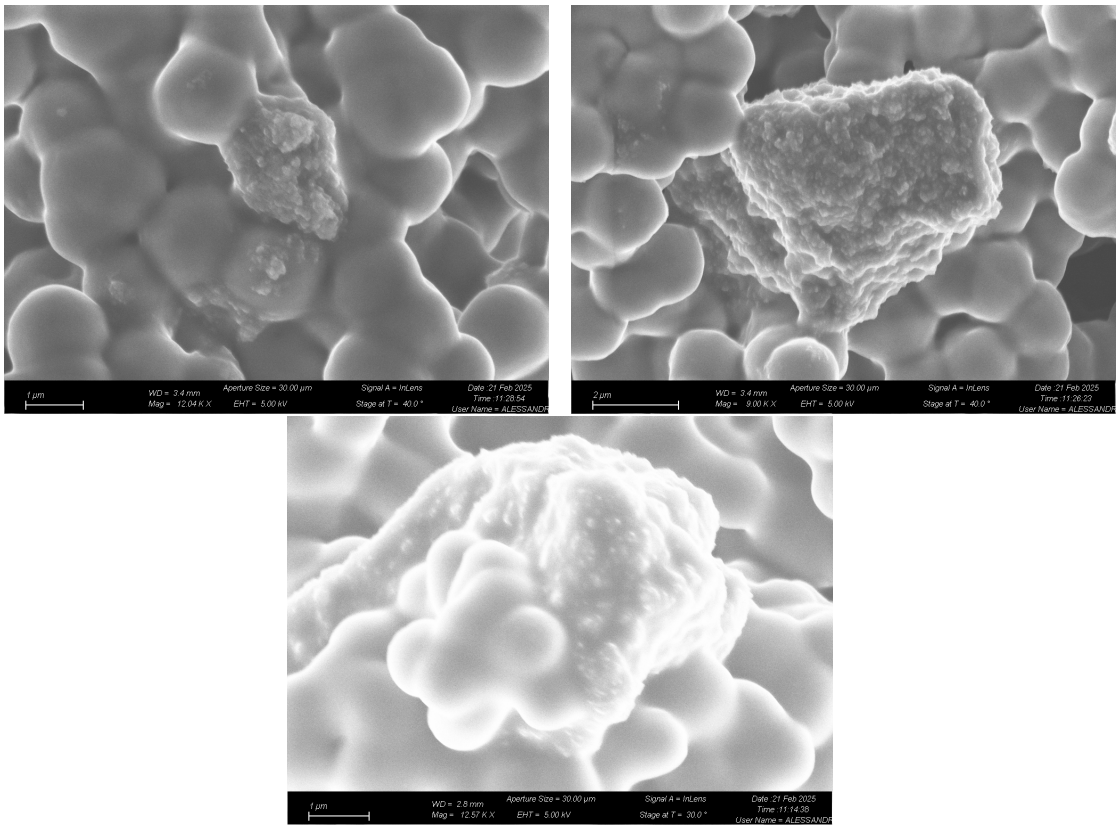

Figure 3.16: FESEM micrographs for SiO_2 nanoparticles.

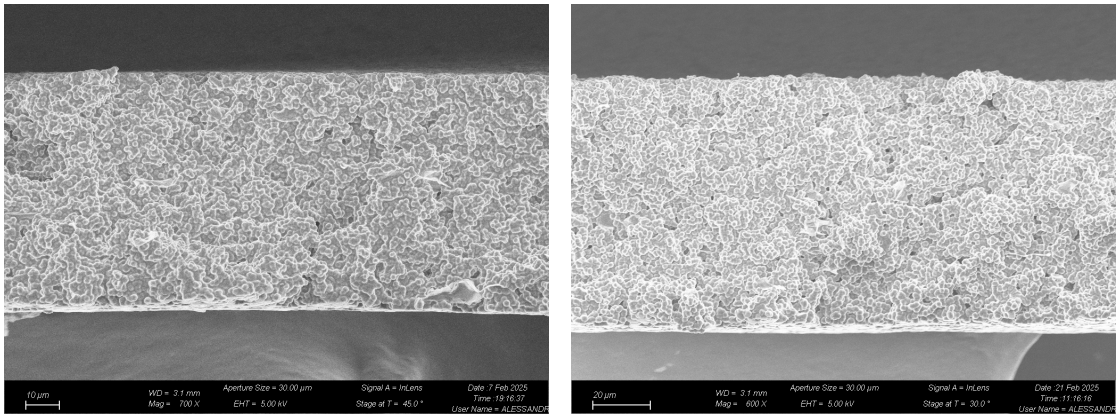

Figure 3.17: FESEM micrographs for IG4 on the left and IG5 on the right.

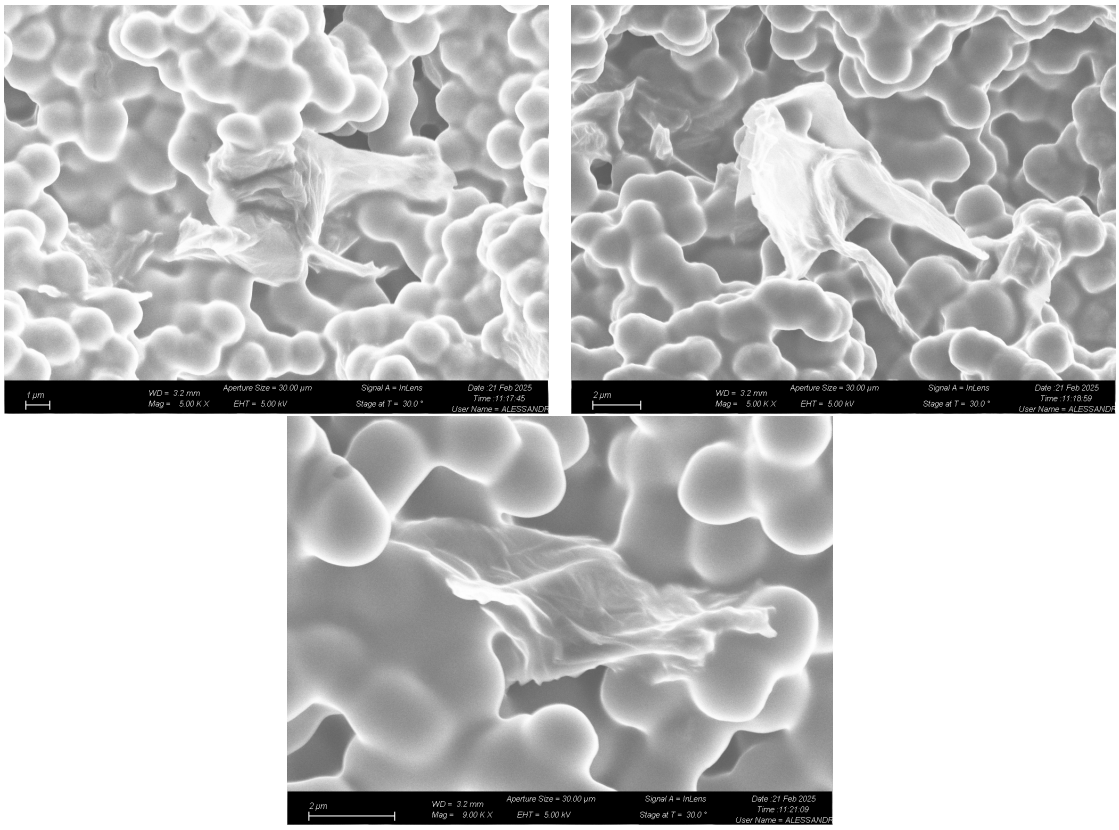

Figure 3.18: FESEM micrographs for GO nanoparticles.

the ion transport process.

A specific setting in the FESEM software was used to obtain a qualitative measurement of the membrane thickness. The results showed that IG1 had a thickness of 47.27 µm, IG2 measured 50.58 µm, IG3 and IG5 both measured 72.80 µm, and IG4 had a thickness of 53.49 µm. The ionogels containing a higher amount of ionic liquid were found to be thicker than the others. This behavior is likely due to a reduced amount of acetone in the solution, which led to less solvent evaporation and consequently more material left after deposition.

3.7 Testing of the EDLCs

As previously mentioned, ten coin cells were fabricated using IG3 and IG5 as both electrolytes and separators. From this point forward, the five coin cells with IG3 as the electrolyte will be referred to as S1, S2, S3, S4, and S5, while those using IG5 will be labeled G1, G2, G3, G4, and G5.

The PEIS analysis was carried out in the range 1 MHz to 10 mHz and the results are plotted as follow: in Figure 3.19 the impedance behaviour of the S serie was plotted at both high and low frequencies, in Figure 3.20 the same criteria is applied to the G serie, in Figure 3.21 a comparison between serie S and G can be witnessed.

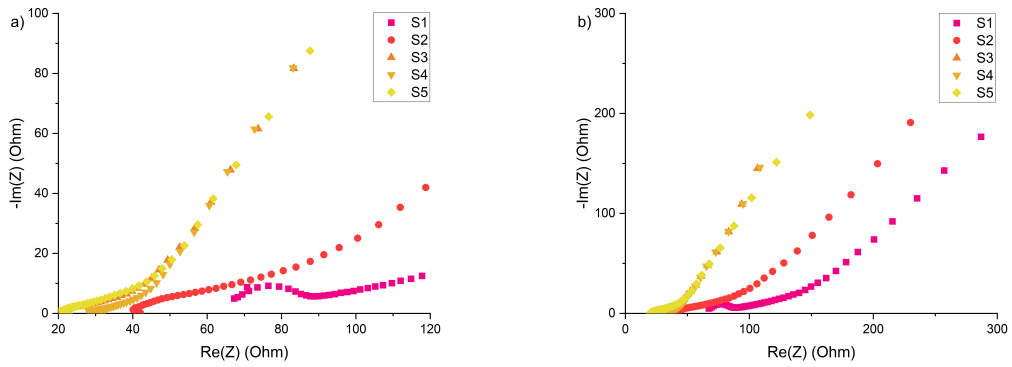

Figure 3.19: PEIS plots for the S serie: a) high frequency region, b) low frequency region.

S5 and G5 were identified as the best performing devices. Their resistance infact resulted to be very low compared to the other devices as already seen in Figure 3.19 and Figure 3.20. To evaluate their behavior at different temperatures, CV analyses were conducted across a temperature range of 5°C to 70°C. Four

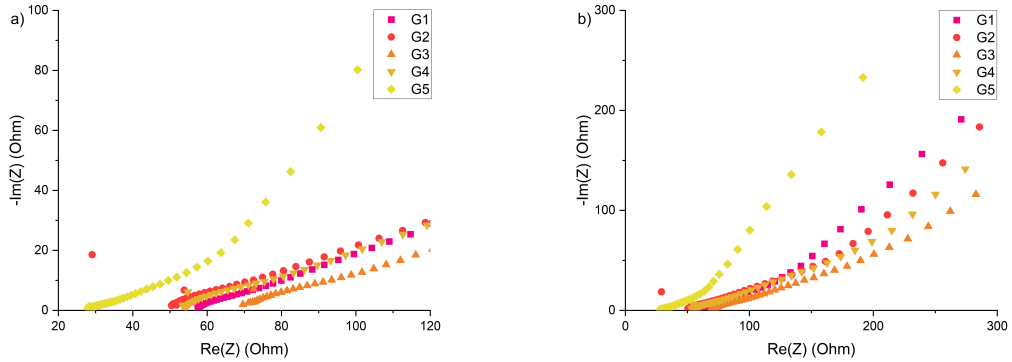

Figure 3.20: PEIS plots for the G serie: a) high frequency region, b) low frequency region.

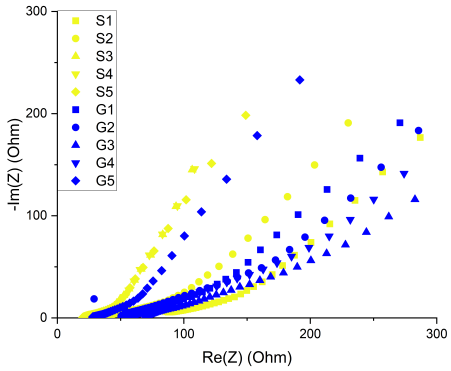

Figure 3.21: Comparison of the impedance between S and G serie.

separate CV analyses were performed at 5°C, 25°C, 50°C, and 70°C for both cells, using a scan rate of 5 mV/s, 50 mV/s and 500 mV/s reaching 2 V. Ten cycles were recorded at each temperature, ensuring the devices had reached a stable state before proceeding.

The results of the CV analysis considering current collectors, two electrodes and the electrolyte are reported in Figure 3.22 for S5 and in Figure 3.23 for G5.

A comparison of the behaviour of the cells at fixed scan rate of 5 mV/s at different temperatures is also reported in Figure 3.24 for both S5 and G5.

From the comparisons, it is evident that S5 outperforms G5 across all tested temperatures and scan rates. This trend appears to contrast with the impedance results of the electrolytes shown in Figure 3.11, where IG3 exhibited better performance

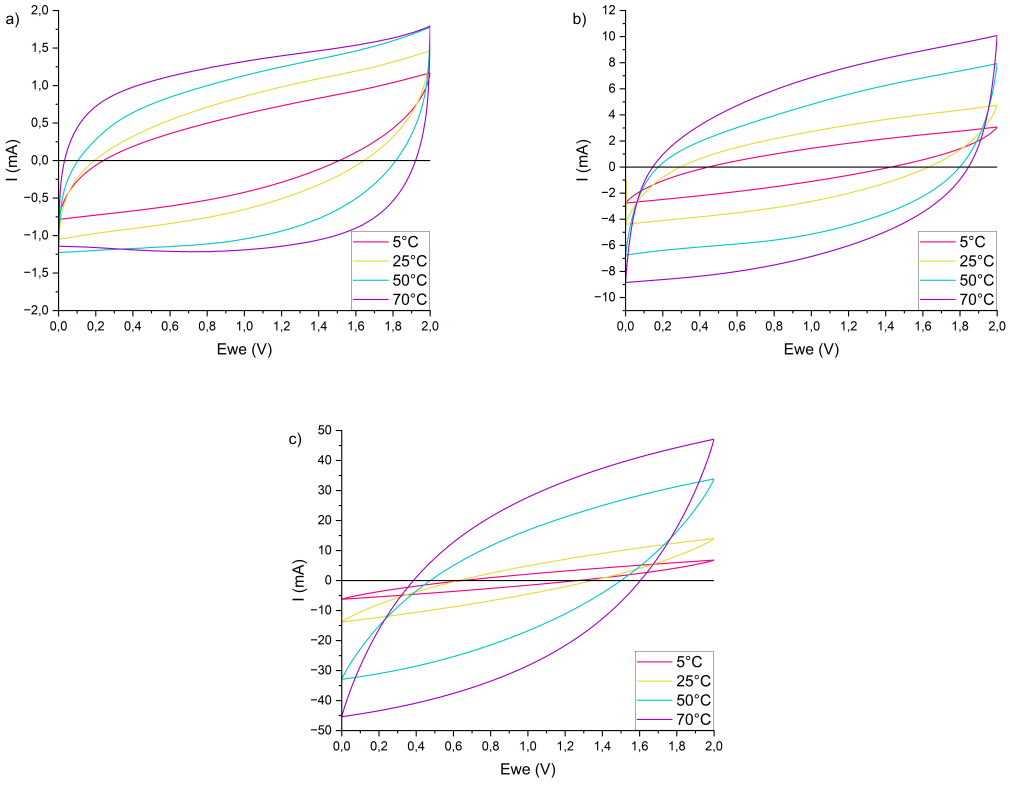

Figure 3.22: CV results considering current collectors, two electrodes and the electrolyte for S5 at different scan rates: a) 5 mV/s, b) 50 mV/s and c) 500 mV/s.

at lower temperatures, while IG5 performed better at higher temperatures. These discrepancies may be attributed to the characteristics of the devices themselves.

The PEIS measurements, reported in Figure 3.19 and Figure 3.20, show that while G5 was the best-performing device within the G series, S5 exhibited lower overall resistance, ultimately resulting in superior performance. Additionally, S5 was also lighter than G5, with the electrodes weighting 10,2 mg and 11,4 mg respectively.

Furthermore, potential interactions between the active carbon electrodes and the silica-based IG or GO-based IG cannot be ruled out as influencing factors, whether positively or detrimentally affecting device performance.

A better understanding of the device behavior can be achieved by normalizing the CV plot with respect to the electrode weight, as shown in Figure 3.25 for both S5 and G5. Table 3.4 and Table 3.5 report the capacitance and normalized capacitance as a function of the active carbon electrode weight.

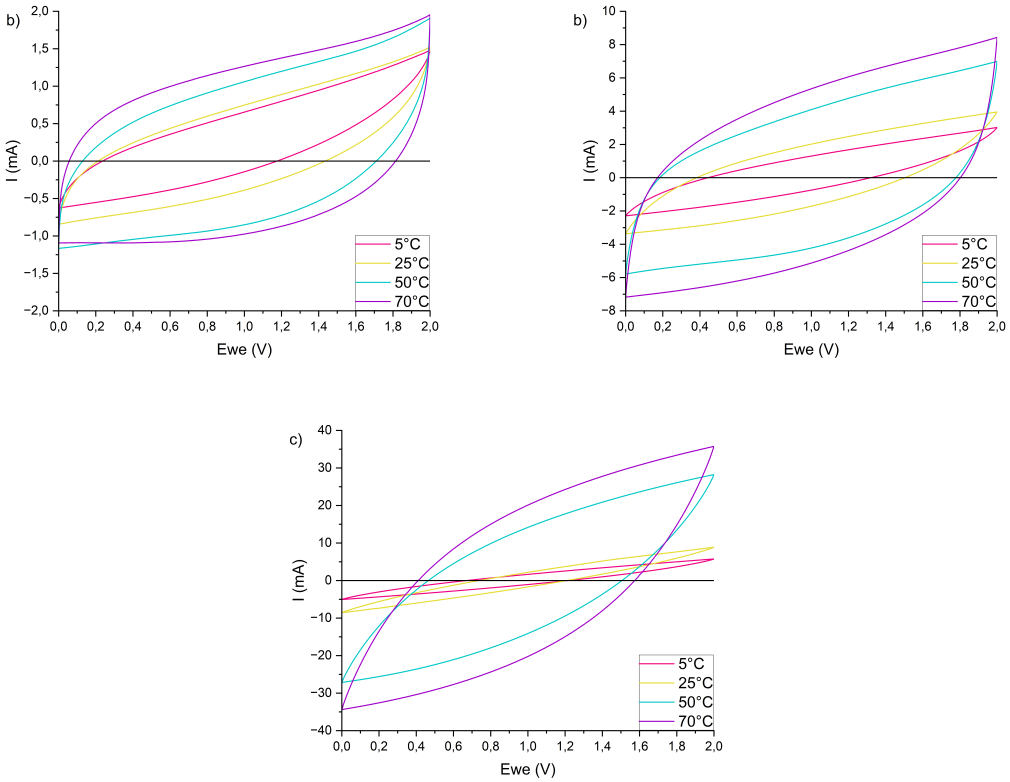

Figure 3.23: CV results considering current collectors, two electrodes and the electrolyte for G5 at different scan rates: a) 5 mV/s, b) 50 mV/s and c) 500 mV/s.

	Scan Rates (mV/s)			**Scan Rates (mV/s)**		
	5	50	500	5	50	500
Temperature (°C)	**Capacitance (F)**			**Normalized Capacitance (F/g)**		
5	0,02243	0,00748	0,00164	2,19946	0,73312	0,16042
25	0,03255	0,01396	0,00390	3,19120	1,36903	0,38189
50	0,04854	0,02497	0,01041	4,75904	2,44795	1,02057
70	0,05657	0,03327	0,01374	5,54645	3,26196	1,34704

Table 3.4: Capacitance and Normalized Capacitance at Different Temperatures and Scan Rates for S5

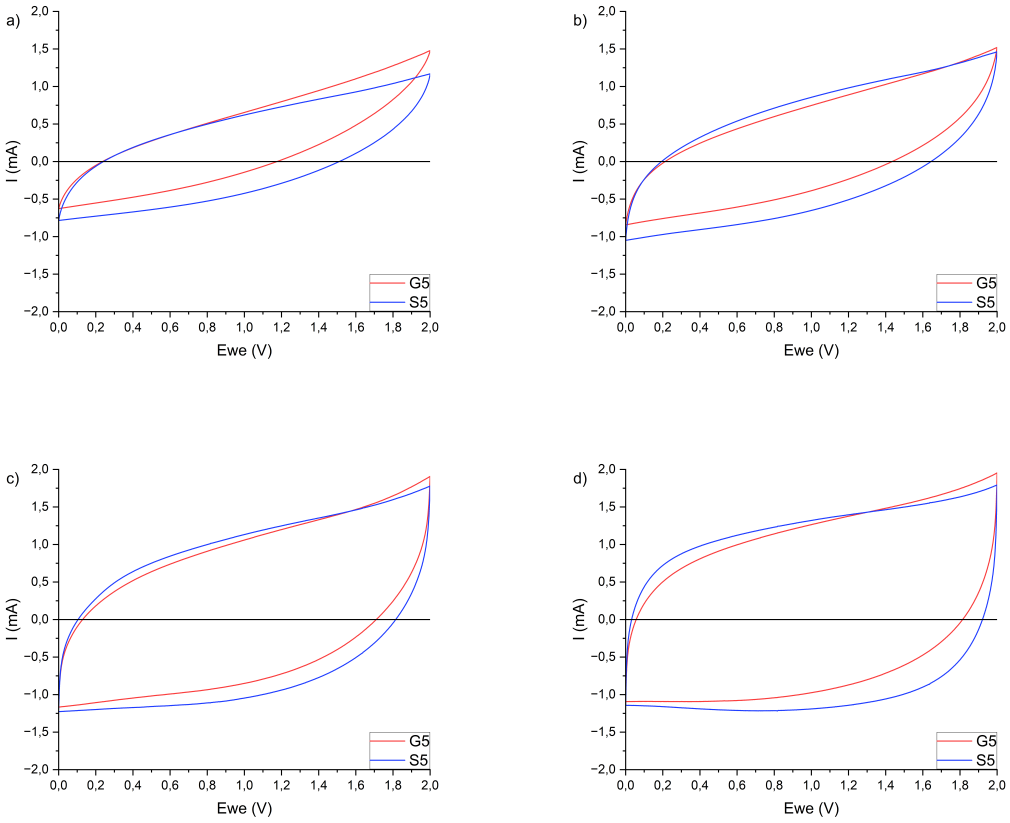

Figure 3.24: CV results comparison between G5 and S5 at a scan rate of 5 mV/s considering current collectors, two electrodes and the electrolyte at: a) 5°C, b) 25°C, c) 50°C and d) 70°C.

	Scan Rates (mV/s)			**Scan Rates (mV/s)**		
	5	50	500	5	50	500
Temperature (°C)	**Capacitance (F)**			**Normalized Capacitance (F/g)**		
5	0,00131	0,00584	0,01334	0,11475	0,51272	1,16980
25	0,02182	0,01010	0,00229	1,91433	0,88630	0,20116
50	0,03985	0,02065	0,00861	3,49523	1,81139	0,75527
70	0,04502	0,02570	0,01138	3,94908	2,25435	0,99845

Table 3.5: Capacitance and Normalized Capacitance at Different Temperatures and Scan Rates for G5

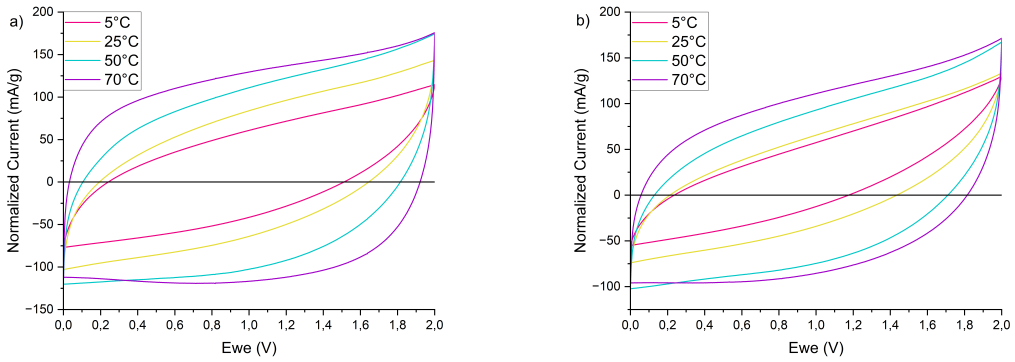

Figure 3.25: Normalized CV plot at 5 mV/s for: a) S5 and b) G5.

Chapter 4

Conclusions and future outlooks

In this study, solid ionogel electrolytes with varying ratios of PVDF-HFP, as the polymer matrix to $Pyr_{14}TFSI$, as the ionic liquid were produced. The effect of introducing silica and graphene oxide nanoparticles into the solutions was also investigated. Membranes made solely of polymer and ionic liquid with ratios ranging from 1:2 to 1:4 were self standing, while the membrane with a 1:5 ratio was too fragile to be peeled off the substrate. The inclusion of nanoparticles improved the structural stability of the ionogels, enabling the production of a self standing 1:5 ratio membrane with both SiO_2 and GO nanoparticles.

TGA was performed to study the thermal behavior, decomposition rates, and maximum working temperature of the electrolytes, which was found to be approximately 200°C. DSC analyses revealed the presence of a "annealing peak" around 70°C, a crucial factor in understanding the electrolytes' electrical behavior.

The viscosity and electrical behavior of three liquid solutions containing the ionic liquid and nanoparticles were also studied to assess the influence of NPs on the ionic liquid's properties. The results demonstrated that the introduction of NPs did not alter the Newtonian behavior of the ionic liquid nor significantly affect conductance, likely due to the low concentration of nanoparticles in the solutions.

PEIS measurements were carried out to determine the conductance of the ionogel electrolytes. IG3 was the best performing membrane at low temperatures, achieving a conductance of 0.308 mS/cm at 5°C. IG5 performed better at higher temperatures, reaching a conductance of 1.454 mS/cm at 70°C. A clear trend was identified: increasing the IL content in the solutions led to higher conductance.

FESEM micrographs of the membranes were obtained to study the morphological structure and nanoparticle dispersion. The ionogel electrolytes exhibited a gel like structure, and no clustering of nanoparticles was observed..

ELDC devices were fabricated using activated carbon as electrodes and IG3 and IG5 as electrolytes, encapsulated in coin cells for testing.

The coin cells underwent PEIS analysis to evaluate their resistance at ambient temperature. S1 and G3, identified as the worst performing devices, were further analyzed using CV at 70°C within a voltage range of 1.5–2.5 V and a scan rate of 5 mV/s to study their behavior.

S5 and G5, the best performing coin cells, were analyzed using CV at 5°C, 25°C, 50°C, and 70°C at various scan rates to understand their performance as a function of temperature.

S5 emerged as the best performing device, consistently outperforming G5 across all temperatures and scan rates. This result contrasts with the electrolyte conductivity analysis, where IG5 exhibited superior performance at higher temperatures. This discrepancy has been attributed to the assembly process of the devices, particularly the amount of active carbon used in the electrodes. A lower mass in a coin cell results in less material overall, reducing resistance and ultimately enhancing performance.

It is important to remember that the ultimate goal of these ionogel electrolytes was their potential implementation in a flexible supercapacitive device, leveraging their self-standing properties and folding capabilities. In this work, coin cells were primarily used to standardize the results, allowing a focused evaluation of the electrolyte performance without concerns about variations in device behavior.

Finally, while functional self standing electrolytes were successfully produced, their conductance was too low for practical applications. To address this, several hypotheses are proposed for future improvement:

i) In this study, simple direct mixing was used. Alternative synthesis methods could yield more homogeneous solutions with better NP dispersion. Automated casting methods could also ensure more uniform membranes compared to those obtained with the Doctor Blade technique.

ii) The max ratio of polymer to IL ratio to obtain a self standing ionogel without NPs was found to be 1:4. Implementing the improvements mentioned above could allow the production of membranes with better ratios, potentially increasing electrolyte capacitance.

iii) A fixed wt% of NPs was used, following the previous studies [52][53]. Varying the wt% could further enhance the ionogels' properties. Additionally, the potential benefits of other types of nanoparticles should not be ruled out.

iv) The setup used for the electrical analyses in this work exhibited higher resistance compared to setups used in the literature, leading to lower conductance values. Using a more optimized setup could yield improved results.

v) A deeper investigation into the temperature dependent behavior of PVDF-HFP is required, particularly concerning the "annealing peak" discussed earlier. Similarly, a more detailed study of the degradation mechanisms of $Pyr_{14}TFSI$ is

essential to fully understand its thermal stability and long term performance.

vi) Sealing the coin cells in a more controlled environment could help minimize the total resistance of the device by preventing parasitic reactions caused by trapped oxygen, thereby improving overall efficiency and stability.

vii) A deeper understanding of the interaction between the selected electrolytes and the electrodes could provide valuable insights for optimizing device performance.

Bibliography

[1] Tyler S Mathis, Narendra Kurra, Xuehang Wang, David Pinto, Patrice Simon, and Yury Gogotsi. «Energy storage data reporting in perspective—guidelines for interpreting the performance of electrochemical energy storage systems». In: *Advanced Energy Materials* 9.39 (2019), p. 1902007 (cit. on pp. 2, 5, 27, 28).

[2] Brian E Conway. *Electrochemical supercapacitors: scientific fundamentals and technological applications*. Springer Science & Business Media, 2013 (cit. on pp. 2, 4, 6).

[3] Alper Tunga Celebi, Matteo Olgiati, Florian Altmann, Matthias Kogler, Lukas Kalchgruber, Julia Appenroth, Ulrich Ramach, Markus Valtiner, and Laura Louise Elizabeth Mears. «Experimental and theoretical understanding of processes at solid-liquid interfaces at molecular resolution». In: *Experimental and theoretical understanding of processes at solid-liquid interfaces at molecular resolution*. Elsevier. 2024, pp. 8–28 (cit. on p. 3).

[4] Maria R Lukatskaya, Bruce Dunn, and Yury Gogotsi. «Multidimensional materials and device architectures for future hybrid energy storage». In: *Nature communications* 7.1 (2016), p. 12647 (cit. on p. 4).

[5] Cynthia G Zoski. *Handbook of electrochemistry*. Elsevier, 2006 (cit. on p. 5).

[6] Somya Samantaray, Debabrata Mohanty, I-Ming Hung, Md Moniruzzaman, and Santosh Kumar Satpathy. «Unleashing recent electrolyte materials for next-generation supercapacitor applications: a comprehensive review». In: *Journal of Energy Storage* 72 (2023), p. 108352 (cit. on p. 6).

[7] Cheng Zhong, Yida Deng, Wenbin Hu, Jinli Qiao, Lei Zhang, and Jiujun Zhang. «A review of electrolyte materials and compositions for electrochemical supercapacitors». In: *Chemical Society Reviews* 44.21 (2015), pp. 7484–7539 (cit. on pp. 7, 8, 10, 11).

[8] Ziyang Song, Ling Miao, Laurent Ruhlmann, Yaokang Lv, Liangchun Li, Lihua Gan, and Mingxian Liu. «Proton-conductive supramolecular hydrogen-bonded organic superstructures for high-performance zinc-organic batteries». In: *Angewandte Chemie International Edition* 62.13 (2023), e202219136 (cit. on p. 7).

[9] Jingjing Yan, Ling Miao, Hui Duan, Dazhang Zhu, Yaokang Lv, Liangchun Li, Lihua Gan, and Mingxian Liu. «High-energy aqueous supercapacitors enabled by N/O codoped carbon nanosheets and "water-in-salt" electrolyte». In: *Chinese Chemical Letters* 33.5 (2022), pp. 2681–2686 (cit. on p. 7).

[10] Elzbieta Frackowiak. «Carbon materials for supercapacitor application». In: *Physical chemistry chemical physics* 9.15 (2007), pp. 1774–1785 (cit. on p. 7).

[11] Nurul Hayati Idris, Md Mokhlesur Rahman, Jia-Zhao Wang, and Hua-Kun Liu. «Microporous gel polymer electrolytes for lithium rechargeable battery application». In: *Journal of Power Sources* 201 (2012), pp. 294–300 (cit. on p. 9).

[12] Lei Qian, Xianqing Tian, Li Yang, Jianfei Mao, Hongyan Yuan, and Dan Xiao. «High specific capacitance of CuS nanotubes in redox active polysulfide electrolyte». In: *Rsc Advances* 3.6 (2013), pp. 1703–1708 (cit. on p. 9).

[13] Ali Eftekhari. «Supercapacitors utilising ionic liquids». In: *Energy Storage Materials* 9 (2017), pp. 47–69 (cit. on p. 10).

[14] Fiona B Sillars, S Isobel Fletcher, Mojtaba Mirzaeian, and Peter J Hall. «Variation of electrochemical capacitor performance with room temperature ionic liquid electrolyte viscosity and ion size». In: *Physical Chemistry Chemical Physics* 14.17 (2012), pp. 6094–6100 (cit. on p. 10).

[15] GP Pandey, Yogesh Kumar, and SA Hashmi. «Ionic liquid incorporated PEO based polymer electrolyte for electrical double layer capacitors: A comparative study with lithium and magnesium systems». In: *Solid State Ionics* 190.1 (2011), pp. 93–98 (cit. on p. 10).

[16] Kanako Yuyama, Gen Masuda, Hiroshi Yoshida, and Takaya Sato. «Ionic liquids containing the tetrafluoroborate anion have the best performance and stability for electric double layer capacitor applications». In: *Journal of Power Sources* 162.2 (2006), pp. 1401–1408 (cit. on p. 10).

[17] Khashayar Ghandi. «A review of ionic liquids, their limits and applications». In: *Green and sustainable chemistry* 2014 (2014) (cit. on p. 10).

[18] Michel Armand, Frank Endres, Douglas R MacFarlane, Hiroyuki Ohno, and Bruno Scrosati. «Ionic-liquid materials for the electrochemical challenges of the future». In: *Nature materials* 8.8 (2009), pp. 621–629 (cit. on p. 10).

[19] Daniel Weingarth, Izabela Czekaj, Zhaofu Fei, Annette Foelske-Schmitz, Paul J Dyson, Alexander Wokaun, and Ruediger Koetz. «Electrochemical stability of imidazolium based ionic liquids containing cyano groups in the anion: a cyclic voltammetry, XPS and DFT study». In: *Journal of The Electrochemical Society* 159.7 (2012), H611 (cit. on p. 11).

[20] Congmin Wang, Huimin Luo, Xiaoyan Luo, Haoran Li, and Sheng Dai. «Equimolar CO 2 capture by imidazolium-based ionic liquids and superbase systems». In: *Green chemistry* 12.11 (2010), pp. 2019–2023 (cit. on p. 11).

[21] John P Canal, Taramatee Ramnial, Diane A Dickie, and Jason AC Clyburne. «From the reactivity of N-heterocyclic carbenes to new chemistry in ionic liquids». In: *Chemical communications* 17 (2006), pp. 1809–1818 (cit. on p. 11).

[22] Ming-Chung Tseng, Huang-Chuan Kan, and Yen-Ho Chu. «Reactivity of trihexyl (tetradecyl) phosphonium chloride, a room-temperature phosphonium ionic liquid». In: *Tetrahedron Letters* 48.52 (2007), pp. 9085–9089 (cit. on p. 11).

[23] L Timperman, A Vigeant, and M Anouti. «Eutectic mixture of protic ionic liquids as an electrolyte for activated carbon-based supercapacitors». In: *Electrochimica Acta* 155 (2015), pp. 164–173 (cit. on p. 11).

[24] Rongying Lin et al. «Capacitive energy storage from- 50 to 100 C using an ionic liquid electrolyte». In: *The Journal of Physical Chemistry Letters* 2.19 (2011), pp. 2396–2401 (cit. on p. 11).

[25] ST Senthilkumar, R Kalai Selvan, and JS Melo. «Redox additive/active electrolytes: a novel approach to enhance the performance of supercapacitors». In: *Journal of Materials Chemistry A* 1.40 (2013), pp. 12386–12394 (cit. on p. 12).

[26] Silvia Roldán Luna, Clara Blanco Rodríguez, Marcos Granda Ferreira, Rosa María Menéndez López, and Ricardo Santamaría Ramírez. «Towards a further generation of high-energy carbon-based capacitors by using redox-active electrolytes». In: (2011) (cit. on p. 12).

[27] Rongyue Wang, Qun Li, Lulu Cheng, Hongliang Li, Baoyan Wang, XS Zhao, and Peizhi Guo. «Electrochemical properties of manganese ferrite-based supercapacitors in aqueous electrolyte: the effect of ionic radius». In: *Colloids and Surfaces A: Physicochemical and Engineering Aspects* 457 (2014), pp. 94–99 (cit. on p. 12).

[28] Madagonda M Vadiyar, Sandip K Patil, Sagar C Bhise, Anil V Ghule, Sung-Hwan Han, and Sanjay S Kolekar. «Improved Electrochemical Performance of a ZnFe2O4 Nanoflake-Based Supercapacitor Electrode by Using Thiocyanate-Functionalized Ionic Liquid Electrolytes». In: *European Journal of Inorganic Chemistry* 2015.36 (2015), pp. 5832–5838 (cit. on p. 12).

[29] Mahbuba Ara, Tiejun Meng, Gholam-Abbas Nazri, Steven O Salley, and KY Simon Ng. «Ternary imidazolium-pyrrolidinium-based ionic liquid electrolytes for rechargeable Li-O2 batteries». In: *Journal of The Electrochemical Society* 161.14 (2014), A1969 (cit. on p. 12).

[30] J Serra Moreno, G Maresca, Stefania Panero, Bruno Scrosati, and GB Appetecchi. «Sodium-conducting ionic liquid-based electrolytes». In: *Electrochemistry communications* 43 (2014), pp. 1–4 (cit. on p. 12).

[31] Laure Dagousset, Giao TM Nguyen, Frédéric Vidal, Christophe Galindo, and Pierre-Henri Aubert. «Ionic liquids and γ-butyrolactone mixtures as electrolytes for supercapacitors operating over extended temperature ranges». In: *RSC advances* 5.17 (2015), pp. 13095–13101 (cit. on p. 12).

[32] Jianmei Lu, Feng Yan, and John Texter. «Advanced applications of ionic liquids in polymer science». In: *Progress in Polymer Science* 34.5 (2009), pp. 431–448 (cit. on p. 12).

[33] Yong-keon Ahn et al. «All solid state flexible supercapacitors operating at 4 V with a cross-linked polymer–ionic liquid electrolyte». In: *Journal of Materials Chemistry A* 4.12 (2016), pp. 4386–4391 (cit. on p. 12).

[34] Ziquan Cao, Hongliang Liu, and Lei Jiang. «Transparent, mechanically robust, and ultrastable ionogels enabled by hydrogen bonding between elastomers and ionic liquids». In: *Materials Horizons* 7.3 (2020), pp. 912–918 (cit. on p. 13).

[35] Jingjing Zhu, Xiaomeng Lu, Wei Zhang, and Xiaokong Liu. «Substrate-independent, reversible, and easy-release ionogel adhesives with high bonding strength». In: *Macromolecular Rapid Communications* 41.24 (2020), p. 2000098 (cit. on p. 13).

[36] Alok Kumar Tripathi, Sevi Murugavel, and Rajendra Kumar Singh. «Dead Ashoka (Saraca asoca) leaves–derived porous activated carbons and flexible iongel polymer electrolyte for high-energy-density electric double-layer capacitors». In: *Materials Today Sustainability* 11 (2021), p. 100062 (cit. on p. 13).

[37] Jean Le Bideau, Lydie Viau, and André Vioux. «Ionogels, ionic liquid based hybrid materials». In: *Chemical Society Reviews* 40.2 (2011), pp. 907–925 (cit. on p. 13).

[38] Hui Jie Zhang et al. «Tough physical double-network hydrogels based on amphiphilic triblock copolymers». In: *Advanced Materials* 28.24 (2016), pp. 4884–4890 (cit. on p. 13).

[39] Ji Wei Suen, Naveen Kumar Elumalai, Sujan Debnath, Nabisab Mujawar Mubarak, Chye Ing Lim, and Mohan M Reddy. «The role of interfaces in ionic liquid-based hybrid materials (ionogels) for sensing and energy applications». In: *Advanced Materials Interfaces* 9.34 (2022), p. 2201405 (cit. on p. 14).

[40] Koichi Fumino, Tim Peppel, Monika Geppert-Rybczyńska, Dzmitry H Zaitsau, Jochen K Lehmann, Sergey P Verevkin, Martin Köckerling, and Ralf Ludwig. «The influence of hydrogen bonding on the physical properties of ionic liquids». In: *Physical Chemistry Chemical Physics* 13.31 (2011), pp. 14064–14075 (cit. on p. 14).

[41] Venkat Ganesan. «Ion transport in polymeric ionic liquids: recent developments and open questions». In: *Molecular Systems Design & Engineering* 4.2 (2019), pp. 280–293 (cit. on p. 15).

[42] Lie Chen, Cong Zhao, Xiaozheng Duan, Jiajia Zhou, and Mingjie Liu. «Finely tuning the lower critical solution temperature of ionogels by regulating the polarity of polymer networks and ionic liquids». In: *CCS Chemistry* 4.4 (2022), pp. 1386–1396 (cit. on p. 15).

[43] Fu Liu, N Awanis Hashim, Yutie Liu, MR Moghareh Abed, and K Li. «Progress in the production and modification of PVDF membranes». In: *Journal of membrane science* 375.1-2 (2011), pp. 1–27 (cit. on pp. 15, 18, 19).

[44] Sreelakshmi Rajeevan, Sam John, and Soney C George. «Polyvinylidene fluoride: A multifunctional polymer in supercapacitor applications». In: *Journal of Power Sources* 504 (2021), p. 230037 (cit. on pp. 16, 18, 20).

[45] Gary D Jones, Roger Alan Assink, Tim Richard Dargaville, Pavel Mikhail Chaplya, Roger Lee Clough, Julie M Elliott, Jeffrey W Martin, Daniel Michael Mowery, and Mathew Christopher Celina. *Characterization, performance and optimization of PVDF as a piezoelectric film for advanced space mirror concepts.* Tech. rep. Sandia National Laboratories (SNL), Albuquerque, NM, and Livermore, CA ..., 2005 (cit. on pp. 17, 18, 20).

[46] Li-Yun Yu, Hong-Mei Shen, and Zhen-Liang Xu. «PVDF–TiO2 composite hollow fiber ultrafiltration membranes prepared by TiO2 sol–gel method and blending method». In: *Journal of Applied Polymer Science* 113.3 (2009), pp. 1763–1772 (cit. on p. 21).

[47] Hui Yang, Joeseph Bright, Banghao Chen, Peng Zheng, Xuefei Gao, Botong Liu, Sujan Kasani, Xiangwu Zhang, and Nianqiang Wu. «Chemical interaction and enhanced interfacial ion transport in a ceramic nanofiber–polymer composite electrolyte for all-solid-state lithium metal batteries». In: *Journal of materials chemistry A* 8.15 (2020), pp. 7261–7272 (cit. on p. 21).

[48] Sobia Farooq, Humaira Razzaq, Shumaila Razzaque, Bilal Ahmad Khan, and Sara Qaisar. «Structural and physical impacts of nanofillers in ionogels: A comprehensive overview». In: *Polymer Composites* 40.S1 (2019), E11–E23 (cit. on p. 21).

[49] Hui Yang and Nianqiang Wu. «Ionic conductivity and ion transport mechanisms of solid-state lithium-ion battery electrolytes: A review». In: *Energy Science & Engineering* 10.5 (2022), pp. 1643–1671 (cit. on p. 21).

[50] Hui Yang, Muhammad Abdullah, Joeseph Bright, Weiguo Hu, Kevin Kittilstved, Yaobin Xu, Chongmin Wang, Xiangwu Zhang, and Nianqiang Wu. «Polymer-ceramic composite electrolytes for all-solid-state lithium batteries: Ionic conductivity and chemical interaction enhanced by oxygen vacancy in ceramic nanofibers». In: *Journal of Power Sources* 495 (2021), p. 229796 (cit. on p. 21).

[51] PeiXia Yang, Lei Liu, LiBo Li, Jun Hou, YanPing Xu, Xuefeng Ren, MaoZhong An, and Ning Li. «Gel polymer electrolyte based on polyvinylidenefluoride-co-hexafluoropropylene and ionic liquid for lithium ion battery». In: *Electrochimica Acta* 115 (2014), pp. 454–460 (cit. on p. 22).

[52] Paulo FR Ortega, João Paulo C Trigueiro, Glaura G Silva, and Rodrigo L Lavall. «Improving supercapacitor capacitance by using a novel gel nanocomposite polymer electrolyte based on nanostructured SiO2, PVDF and imidazolium ionic liquid». In: *Electrochimica Acta* 188 (2016), pp. 809–817 (cit. on pp. 22, 50, 66).

[53] Xi Yang, Fan Zhang, Long Zhang, Tengfei Zhang, Yi Huang, and Yongsheng Chen. «A high-performance graphene oxide-doped ion gel as gel polymer electrolyte for all-solid-state supercapacitor applications». In: *Advanced Functional Materials* 23.26 (2013), pp. 3353–3360 (cit. on pp. 23, 50, 66).

[54] Alexandros Ch Lazanas and Mamas I Prodromidis. «Electrochemical impedance spectroscopy a tutorial». In: *ACS Measurement Science Au* 3.3 (2023), pp. 162–193 (cit. on p. 27).

[55] EL-CELL GmbH. *EL-CELL Electrochemical Test Equipment*. `https://el-cell.com/products/test-cells/standard-test-cells/ecc-std/`. Accessed: 2025-02-014. 2025 (cit. on p. 31).

[56] Keisei Suzuki, Kenichi Ikari, and Hiroaki Imai. «Synthesis of silica nanoparticles having a well-ordered mesostructure using a double surfactant system». In: *Journal of the American Chemical Society* 126.2 (2004), pp. 462–463 (cit. on p. 32).

[57] KURARAY COALTM. *YP Series: Fine Activated Carbon for Energy Storage.* Available online: `https://www.calgoncarbon.com/app/uploads/YP-brochure-draft_final_08_2019.pdf` (Accessed: March 10, 2025). 2025 (cit. on p. 32).

[58] Marie Gabard, Mustapha Zaghrioui, David Chouteau, Virginie Grimal, Thomas Tillocher, Fouad Ghamouss, and Nathalie Poirot. «Novel method based on spin-coating for the preparation of 2D and 3D Si-based anodes for lithium ion batteries». In: *ChemEngineering* 1.1 (2017), p. 5 (cit. on p. 46).

[59] Michael Neidhöfer, Francois Beaume, Laurent Ibos, Alain Bernes, and Colette Lacabanne. «Structural evolution of PVDF during storage or annealing». In: *Polymer* 45.5 (2004), pp. 1679–1688 (cit. on p. 48).